J. Webster (ed.), *Wiley Encyclopedia of Electrical and Electronics Engineering*

VACUUM MICROELECTRONICS

Historically, field-emission cathodes were conceived as a substitute for the thermionic cathodes of conventional microwave tubes (1). This application has driven much of the subsequent development of field-emitter arrays (*FEAs*) and has spawned the field of vacuum microelectronics, in which microlithography is used to fabricate FEA cathodes for such amplifiers. The notion of vacuum microelectronics has since expanded to include display applications (2,3,4,5,6,7,8,9), such as the use of field emitters in flat-panel displays (see Field Emission).

However, the focus of this article will be on the progress toward the realization of an FEA–cathode microwave amplifier and the development and status of FEAs in this context. Variants of the traveling-wave tube (*TWT*) and the klystron will be discussed in detail, and the potential advantages of such devices over other tubes and solid-state devices will be described. This article presents both the physical principles that underlie the issues and the simple mathematical analyses that describe them.

Microwave Amplifiers and Vacuum Microelectronics

It can be shown (10,11) that, for triode- and transistor-like three-terminal devices, the maximum power P_m that can be delivered to a load is

$$P_m = \frac{E_m^2 v_s^2}{X_o (2\pi f_T)^2} \tag{1}$$

where E_m is the critical field at which electrical breakdown will occur, v_s is the velocity of electrons through the device, X_o is output impedance level, and f_T is the cutoff frequency. Equation (1) can be used to understand the difference between solid-state and vacuum devices. In a solid-state device, f_T can be quite high because device dimensions can be made small by using microlithographic techniques. However, the electron velocity in a solid-state device cannot exceed approximately 10^7 cm/s because of electron collisions with the semiconductor lattice, whereas for vacuum tubes even relativistic velocities can be attained. The breakdown process in a semiconductor is initiated by transitions from the valence to conduction bands, which typically require energies only on the order of 1 eV. In contrast, breakdown in tubes is determined by secondary-emission processes that can be minimized by proper choice of materials and geometry. Furthermore, the heat that must be dissipated in the semiconductor more stringently limits the output power in a solid-state device. In general, semiconductors have much lower thermal conductivity than metals, so that a properly designed microwave tube can provide better thermal paths to dissipate heat. Consequently, for quite fundamental reasons, the output power provided by a microwave tube can be much higher than that provided by a solid-state device.

The triode, the first microwave tube, was invented in 1906 by Lee de Forest. In a triode, the electron beam is modulated by a grid and collected by a plate (anode) that is connected through a load to ground. The classical high-frequency vacuum triode reached maturity in the late 1940s with the "lighthouse" family of cavity-driven, gridded tubes (12 13 14,15). The lightouse design minimized parasitic losses by making all high-frequency

connections radially through disk leads. The 416A triode operated to 4 GHz. Its grid was 90 mil (2.3 mm) in diameter, was fabricated from a 0.3 mil (7.6 μm) tungsten wire wrapped at 1000 turns per inch, and was mounted 0.6 mil (15 μm) above the cathode surface. The variation in wire spacing and grid–cathode spacing was less than 10%, although the cathode diameter was 150 times the grid–cathode spacing. Measurements indicated that the 416A triode was within a factor of 5 of the theoretical maximum performance imposed by the thermal velocity spread of electrons emitted by a thermionic cathode. The power-handling capability of the grid structure posed the most severe limitation to further extensions of the frequency range. The stiffness of the grid wires limited the diameter of the cathode (and so the diameter of the beam), and interception of beam current by the grid limited the maximum current density to about 180 mA/cm^2. At 4 GHz, the 416A triode achieved a gain of 10 dB with an instantaneous bandwidth of 2.5%. Transit-time effects also limited the frequency response of these triodes.

As discussed later, the transit time of electrons through the region of a triode (or pentode) in which the grid fields interact with the electrons must be less than the period of the electromagnetic radiation. Further advances in the gain–bandwidth product of the 416A tube would have required a grid–cathode spacing of less than 0.2 mil (5 μm). The fabrication of such a tube would be quite challenging, and even if it were feasible, the high cathode operating temperatures (on the order of 700°C to 800°C) would create thermal expansion and reliability problems on the nearby grid. Since a reduction in grid–cathode spacing increases the grid–cathode capacitance, the lateral dimensions of the cathode must be reduced as well, which further reduces the peak power. Subsequent development shifted to linear-beam velocity-modulated (klystrons, *TWTs*) and crossed-field devices.

As the operation frequency extends above about 500 MHz, the wavelength of the signal becomes comparable to the dimensions of the circuit, so that circuit elements in conventional microwave tubes become distributed. Capacitors can no longer be modeled as capacitors, inductors no longer appear inductive, and transit-time effects occur. Only by reducing the physical size of the elements can such distributed effects be eliminated. In no element is this size reduction more profitable than the part of the tube that produces the electrons, the cathode. In contrast, miniaturization of the output circuit tends to reduce its power-handling ability and thus limit the average power of the amplifier. In a field-emission cathode, a cathode heater is absent, and the input signal and emitted beam dissipate only a moderate amount of heat in the cathode region.

In contrast to the triodes just discussed, klystrons and TWTs utilize inductive circuits to exchange energy with the electron beam. Electron transit times that are long compared to the period are not problematic because the high-frequency coupler is distinct and separate from the beam emission and collection circuit. The electron beam does not strike the radio frequency (*RF*) output circuit as it does in a resistive output circuit; rather, it is decelerated by passing through a traveling or standing electromagnetic wave that is developed in an output circuit. Such an inductive output circuit can be many wavelengths long, allowing a cumulative interaction that converts part of the kinetic energy of the beam into electromagnetic energy in each period. Only after the complete extraction of high-frequency power is the spent beam dumped into a collector. As shown in Fig. 1(a) the electron beam that is emitted by the cathode is not modulated (a "dc beam"). In the first section of the circuit, the RF input signal imposes a small velocity modulation ($v = v^{\mathrm{dc}} + v^{\mathrm{RF}}$) on the electron beam, which launches longitudinal space-charge waves. In these waves, the beam modulation cycles each plasma wavelength between kinetic-energy modulation, that is, velocity modulation, and potential-energy modulation, that is, density modulation ($n = n^{\mathrm{dc}} + n^{\mathrm{RF}}$), as the electrons drift through the microwave tube. If the initial modulation is small, it is increased by passing the beam through intermediate interaction regions where RF ripples in the beam current enable energy to be exchanged with an electromagnetic wave. In the last interaction region (the output region), the relative phase of the plasma wave and the electromagnetic wave is adjusted to maximize energy transfer from the beam to the electromagnetic wave.

Appropriate interaction circuits include resonant cavities and structures that will support a slow electromagnetic wave with a phase velocity close to the beam velocity. Two extreme cases are the pillbox cavity and the helical coil; the amplifiers that use them are the narrow-band, high-gain klystron and the wide-band, lower-gain helix TWT, as will be discussed in more detail later. Amplifiers with intermediate gain and bandwidth use

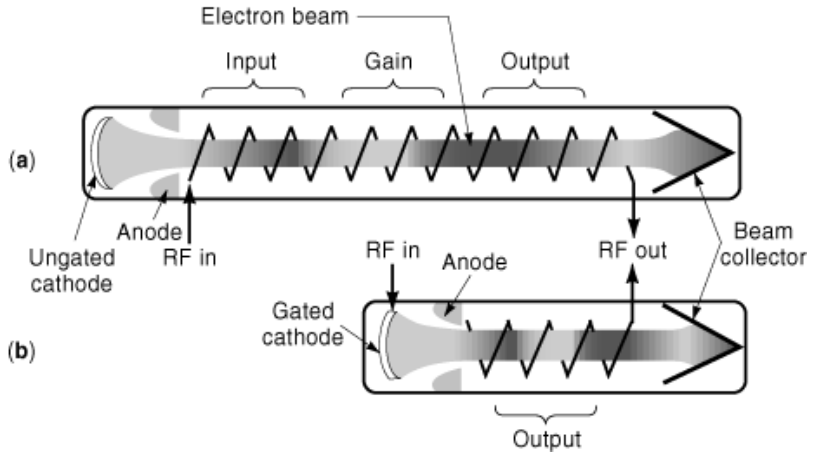

Fig. 1. (a) Traveling-wave tube (*TWT*) and (b) twystrode. The twystrode's gated cathode replaces the input and gain sections of the TWT by modulating the emitted beam current.

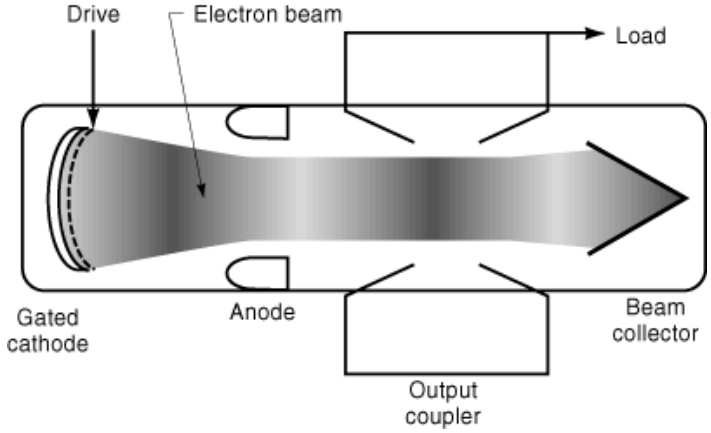

Fig. 2. Klystrode. A field-emission cathode provides a density-modulated beam. RF energy is extracted from the accelerated beam by the output coupler, which is a resonant cavity, and the spent beam is recovered in a beam collector.

circuits such as the various coupled-cavity and ring-bar structures. In all of these velocity-modulated tubes, approximately the first two-thirds of the length of the circuit is employed in achieving a strong modulation of the beam, with the last one-third allocated to extracting output power. The higher the desired gain, the longer the circuit must be to convert a very small input signal into a large RF modulation of the electron-beam current. The electron beam must be magnetically focused over the whole length of the interaction circuit, which makes velocity modulation an expensive approach in terms of size and weight.

In variants of these tubes, the klystrode and twystrode, velocity modulation is replaced by density modulation from a gated cathode that emits a directly modulated electron beam. A twystrode, as illustrated in Fig. 1(b), combines a gated cathode, in which the input signal modulates the beam density, with a wide-band output circuit in which the modulated beam interacts with a synchronous electromagnetic wave. The device is analogous to a TWT with the inductive input circuit replaced by a gated cathode. The gated cathode must be embedded in a broadband input circut to realize the full bandwidth potential of the broadband output circuit. A klystrode, as illustrated in Fig. 2 is a narrow-band, high-gain amplifier consisting of a gated cathode

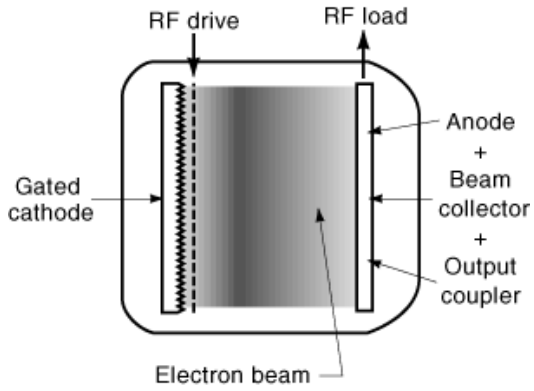

Fig. 3. Vacuum microtriode. A RF signal is applied to the gate electrode of the field-emitter array, providing a density-modulated beam. The anode both collects the beam and delivers amplified current to the RF load.

modulated by the input signal followed by a resonant-cavity output circuit. Klystrodes and twystrodes thus combine the best features of triodes and velocity-modulated tubes. A gridded cathode imposes a strong initial density modulation on the beam current, eliminating approximately two-thirds of the size and weight of the tube, while the inductively coupled output circuit provides high power-handling capability and high efficiency. Although density modulation of electron beam offers clear advantages in efficiency and compactness, it makes stringent demands on the cathode structures that provide the emission gating.

The conventional gated cathode is a grid-controlled thermionic cathode. However, such cathodes are limited in high-frequency response by transit-time effects, high grid–cathode capacitance, and low transconductance. The spacing of the grid–cathode gap and the transparency of the grid are critical limitations imposed by fabrication technology and material properties. At common operating voltages and at frequencies above 1 GHz, structures smaller than 10 μm must be fabricated to tolerances of 10% or less. Grid materials must possess good thermal and electrical conductivity, excellent mechanical stability at temperatures above 1000°C, and low secondary-electron emission ratios. The most common materials meeting these requirements are tungsten or molybdenum, possibly coated with noble metals. Graphite, an early contender that was dropped because of excessive fragility, has returned in the form of pyrolytic graphite.

Microelectronic FEAs can modulate the beam density at high frequency and with good spatial localization, extending the frequency range of density-modulated amplifiers by orders of magnitude. Microelectronic FEA structures overcome the limitations of gridded thermionic cathodes by having the grid (or gate) in nearly the same plane as the emitters, dramatically reducing interception current and increasing transconductance. A microtriode using an FEA cathode is illustrated in Fig. 3 The use of field emission also eliminates the need for dispensing a continuous supply of low-work-function material that vaporizes in the tube. This material can coat the grids of thermionic cathodes and the surface of grid–cathode insulators, resulting in secondary emission and shorts.

The principal advantages of microfabricated FEAs are the negligible tip-to-gate transit time and the high transconductance. FEA cathodes require no heater power, offer 'instant on' capability because there is no delay while the cathode is heated, can provide extremely high current densities, and can be operated at high pulse repetition rates. Consequently, incremental performance improvements are obtained in even conventional velocity-modulated amplifiers when an ungridded thermionic cathode is replaced by an FEA cathode that produces an unmodulated electron beam. FEAs have been used as cathodes in velocity-modulated fast-wave (16) and slow-wave (17 18 19,20) devices. However, a gated FEA cathode that provides a density-modulated beam current at the input of an amplifier enables amplifiers with substantial qualitative advantages over

both velocity-modulated and conventional gated-cathode amplifiers. Because of improvements in gated-FEA technology, such cathodes are feasible alternatives to thermionic electron beam sources (21 22,23) for emission gating at frequencies above ultrahigh frequencies (*UHFs*). This new opportunity, however, depends critically upon the ability to integrate the gated-FEA technology into the vacuum-tube environment.

To summarize, inductive output amplifiers (*IOAs*) (24) use a gated cathode to modulate the current and an inductively coupled output circuit, where the beam interacts with a resonant or synchronous electromagnetic wave to couple power from the beam. In this class of devices, the beam is fully modulated before it is accelerated by the anode, no drift space is needed to convert velocity modulation into density modulation, and the RF output electrode(s) are separate from the beam-collection electrodes. The absence of an inductive input circuit and its associated length of magnet make IOAs potentially more compact and higher in specific power (W/g) than their analogous velocity-modulated amplifiers. Additionally, in contrast to velocity-modulated tubes, IOAs can operate as power amplifiers in Class B or C.

In an IOA, in contrast to other linear-beam tubes, the modulated beam is the only conveyor of information about the input signal to the output circuit of the tube. This results in a physical isolation of the input circuit, which dominates the gain, from the output circuit, which controls the efficiency. The design criteria for the cathode and the output circuit are thus clearly distinguished. The role of the gated cathode and its impedance-matching circuit is to produce an electron beam of the desired current waveform using a minimum of input signal power over the desired frequency band. The role of the output interaction circuit is to convert beam energy efficiently to electromagnetic energy at the desired frequency in as short a circuit length as possible. Inductive output amplifiers are classified according to the type of output interaction: klystrodes use a standing-wave cavity and twystrodes use a traveling-wave circuit.

Field Emitter Arrays

Operation and Fabrication. The key to the performance advantages of IOAs is the emission gating of the electron beam at the cathode surface before acceleration to anode potential. The cathode assembly that performs this modulation is usually an old technology pushed to its fundamental limitations (i.e., gridded thermionic cathodes) or a new technology pushed to its present limits of performance (i.e., FEAs or laser-driven photocathodes). The critical measures of the performance of any emission-gated cathode are low transit time, high transconductance, low capacitance, and current density that is sufficiently high for good performance, but not too high for good beam optics. Each of these factors is reviewed in the following.

In order to extract electrons from a metal or semiconductor into a vacuum, the potential-energy barrier that confines electron to the metal, the work function ϕ, must be overcome by external means. The situation, absent any such physical means, is illustrated by Fig. 4(a) In thermionic cathodes, the host cathode metal is heated until the thermal energy of the electrons allows their escape, as is illustrated by Fig. 4(b). Very high temperatures are required for this purpose, on the order of 700°C to 800°C, and emission from such thermal cathodes cannot be modulated at microwave frequencies.

In field-emission cathodes, the electrons are extracted by high electric fields, as illustrated by Fig. 4(c). In this case, the width of the confining potential barrier is reduced by the external electric field, which allows a significant fraction of the electrons to escape by quantum-mechanical tunneling. The emission process can be described by the Fowler–Nordheim relationship (25), which gives the emitted current density J (A/cm^2) as a function of the electric field E_T (V/cm) normal to the emitting surface. This relationship can be approximated (26) as

$$J = 1.5 \times 10^{-6} \frac{E_T^2}{\phi} e^{10.4/\phi^{1/2}} e^{-6.44 \times 10^7 \phi^{3/2}/E_T} \qquad (2)$$

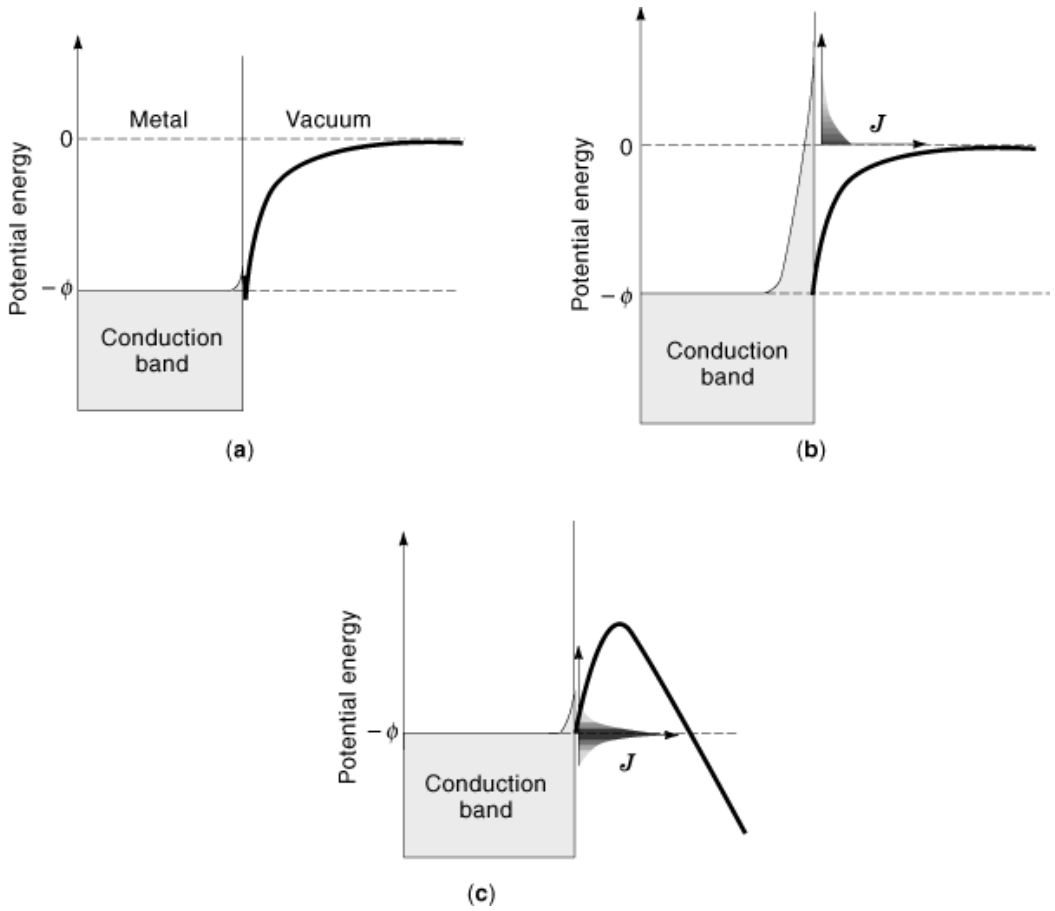

Fig. 4. Emission processes. (a) Potential energy of electrons at a metal–vacuum interface in the absence of any external stimuli. The electrons are confined in the metal by a potential barrier ϕ that must be overcome to extract electrons into the vacuum. (b) Thermionic emission. The cathode is heated to temperatures exceeding 700°C, allowing thermally excited electrons to escape from the metal. (c) Field emission. The application of a high external electric field diminishes the width of the potential barrier that confines the electrons, which allows them to escape by quantum-mechanical tunneling. This process is usually well described by the Fowler–Nordheim relationship.

For most metals, $\phi \cong 4$ eV. It is evident from (Eq. 2) that very high electric fields, on the order of 10^8 V/cm, are required for emission. Impracticably high voltages are required to attain such fields between simple parallel-plane electrodes. For example, a voltage of 1000 kV is required to achieve a field of 10^8 V/cm between two such electrodes spaced apart by 100 μm, a value that would cause arcing between the electrodes. Consequently, the required electric fields must be achieved by utilizing the field enhancement that occurs at a sharpened metallic tip. A typical gated FEA is shown in Fig. 5 To produce FEAs, solid-state electronic fabrication techniques are used to form conical emitter tips of semiconductor or metal materials on an appropriate substrate, for example, doped or undoped silicon. A metal gating electrode is fabricated in close proximity to the tips, typically supported by an insulating layer such as SiO_2. Electrons are emitted from the surface in response to extremely high fields that are created at the emission tip by the voltage on the gate electrode. The electrons' momenta carry them quickly out of the strong field region where they are captured by the anode field and accelerated away from the field-emission structure. In most cases, the anode is much further away from the tips than the gate electrode,

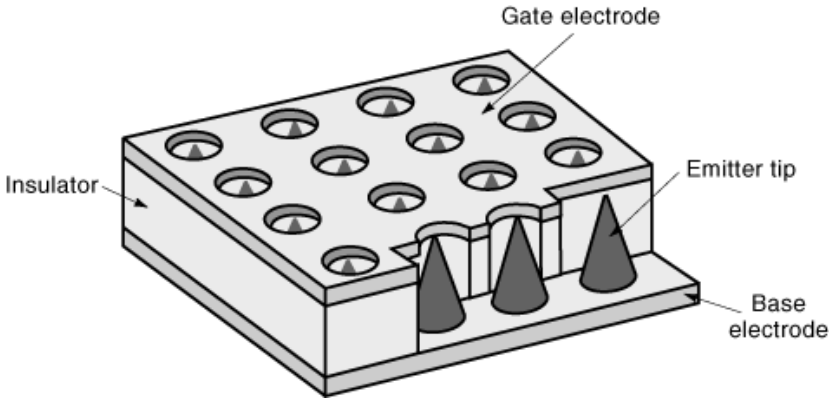

Fig. 5. Drawing of field-emitter array. Using microelectronic fabrication techniques, an array of sharply pointed tips with a gate electrode in close proximity can be fabricated. Typically, the tips are spaced 0.3 μm to 2 μm apart and are 0.2 μm to 1 μm high. Radii of curvature at the tip range from 100 Å to 1000 Å. High tip fields are achieved by applying a positive voltage difference between the gate electrode and the tips, typically in the range of 50 V to 150 V. After the electrons are extracted from the cathode, they electrons can be formed into a useful beam by the anode electric field and an external magnetic field.

so that the electric field at each tip is primarily determined by the gate-tip voltage V_G. The small size and high initial accelerating field leads to insignificant transit-time effects, as discussed later.

If effects related to the space charge of the emitted electrons are neglected, E_T is proportional to V_G, that is $E_T = \beta_T V_G$. Equation (2) can then be used to describe the emission current I_B as

$$I_B = AV_G^2 e^{-B/V_G} \tag{3}$$

If the emitters are identical, and N_T is the number of tips in the array and A_T is the effective area of emission for each tip, the parameters A and B are given by

$$A = N_T A_T \frac{1.5 \times 10^{-6} \beta^2}{\phi} e^{10.4/\phi_0^{1/2}}$$

$$B = \frac{6.44 \times 10^2}{\beta} \phi^{3/2}$$

The parameters A and$B$ are usually determined experimentally by the slope and intercept of a plot of ln (I/V^2_G) versus $1/V_G$, a plot usually referred to as a Fowler–Nordheim plot (27). As discussed later, individual emitting tips are rarely uniform across an array. Consequently, the expression for the parameter A is usually of limited value in interpreting experimental data. The field-enhancement factor β_T can be approximated by (28).

$$\beta_T = \frac{R}{kr(R-r)} \tag{4}$$

In (Eq. 4), r is the radius of curvature of the tip, R is the tip–gate distance, and k is a constant that typically ranges from 1 to 5, depending on the tip geometry.

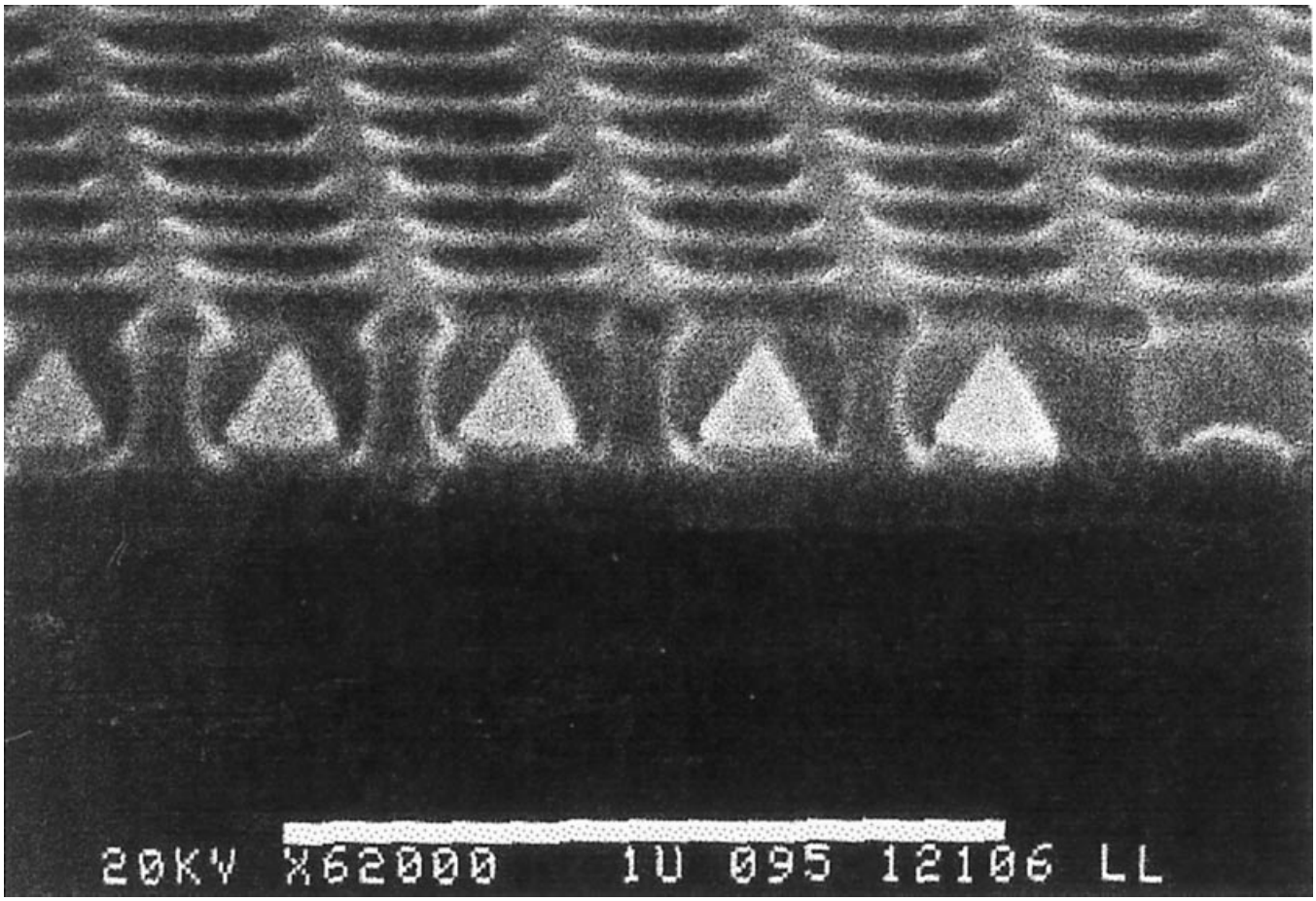

Fig. 6. Scanning electron micrograph of a field-emitter array. The tips are arrayed with a 0.32 μm periodicity, corresponding to a density of 10^9 tips/cm^2. Interferometric laser lithography was used to achieve the small tip sizes. The conical Mo tips are 2000 Å high with tip radii of approximately 100 Å.

Planar fabrication processes have been used to fabricate a variety of FEAs, including arrays with Mo (19,21,24 25 26,27,29 30,31,32,33,34), Si (35,36,37), GaAs (38), and GaN (39,40) tips. Arrays having a tip density as large as 10^9 tips/cm^2 have been fabricated (31). A scanning electron micrograph of such an array density of is shown in Fig. 6 Several research groups have reported gated-FEA emission currents that are sufficitly large for application to microwave tubes (21,33).

The physical emission processes involved in emitters as presently fabricated are far more complex than the simple model described above. It is well known that the characteristics of field emitters depend upon a number of environmental factors, such as vacuum quality and the cleanliness of neighboring structures (41,42,43,44). Unfortunately, high-temperature desorption of contaminants is often the only technique that can completely clean the field-emitter tips in an array, but this is precluded by the diverse materials used to fabricate a FEA. In addition, the surfaces of metallic field emitters are not perfectly smooth, as assumed by (Eq. 2). Instead, the surfaces are populated with atomic-scale "nanotips" that further increase the nearby electric field (45).

A body of evidence (45,46,47,48) indicates that emission occurs primarily at a subset of these sites. It appears that the time variation of the constituents and character of this subset can often account for the

complex behavior observed in experimental FEAs. These include the lengthy conditioning procedures that are necessary to stabilize and increase emission (48), noise properties of the emitters, and premature burnout (30,48). Studies of how emission current and noise scale with array size show that only a small fraction of the tips in an array participates in electron emission (44,49). Consequently, the actual business of operating emitters involves a number of empirical procedures that are not well understood. A major part of the challenge in applying FEAs to IOAs is the development and adaptation of conditioning procedures for the tube environment.

Noise Characteristics. A thermionic cathode is usually operated in a space-charge-limited mode; that is, the emission current is limited by the field associated with the charge in the cathode–anode region, not by the ability of the cathode to supply electrons. Consequently, noise waveforms that are inherent to the cathode emission process do not strongly appear in the electron beam. In contrast, a FEA cathode is not usually operated in a space-charge-limited mode, because the presence of appreciable space charge causes emitted electrons to be reflected to the microfabricated grid. The reflected electrons induce gate current, which degrades both the reliability and operating characteristics of the FEA. Absent the stabilizing effect of the space charge, fluctuations in FEA emission current can adversely affect tube performance.

The emission current from FEAs is dominated by burst noise (50,51), which is alternatively called random-telegraph or popcorn noise. Other forms of the ubiquitous "1/ f noise" have also been observed (44), as well as shot noise and thermal noise, but they are typically negligible compared to burst noise for $f < 1$ kHz. Burst noise consists of current pulses of randomly distributed lengths at randomly distributed times that are superimposed upon the emission current. Often the pulses have nearly equal amplitude, but occasionally the amplitudes are distributed between several levels. The physical explanation for burst noise in field emitters is not known with certainty, but burst noise can be caused by any affect that randomly modulates the emission current (50). Examples of such effects are the appearance and disappearance of nanoprotrusions, field-aided migration of impurities, or adsorption or desorption of gases. If the burst-noise waveform is bistable, and the transitions between levels are assumed to follow Poisson statistics, the noise power spectral density $S_1(\omega)$ is given by (50)

$$S_1(\omega) = \frac{8\nu\Delta I^2}{4\nu^2 + \omega^2} \tag{5}$$

In (Eq. 5), ΔI is the magnitude of the current pulses and ν is the mean number of transitions per second. Experimentally, the low-frequency noise can be described by a power spectral density of

$$S(f) = \frac{\text{const}}{f^\gamma} \tag{6}$$

The quantity γ is referred to as the spectral density index, and is usually between 1 and 2 (26,44,52) for field emitters. The baseband flicker noise may modulate the microwave signal, producing phase noise and adversely affecting its spectral purity. The effects of these noise sources upon TWT operation have not been studied experimentally because of the limited life of previous FEA TWT amplifiers. Consequently, the conversion efficiency of the low-frequency flicker noise to the microwave frequency of the amplifier has not been measured.

In recent measurements, workers at the Massachusetts Institute of Technology Lincoln Laboratory have measured the baseband spectrum from FEAs that are comparable to those used in the klystrode tests (49). Initial tests indicate that γ is typically between 1.7 and 1.9, and that over 99% of the noise power exists below 20 Hz with over 90% concentrated below 2 Hz. Similar results have also been found in another study using Si emitters (44). The low-frequency nature of the noise power bodes well for the use of FEAs in microwave power tubes. For example, one would not expect broadening of a 10 GHz carrier signal by more than ±20 Hz,

which should not interfere with any practical voice-communication or radar application (including most Doppler systems).

Modulating a Gated FEA. To achieve acceptable gain in an IOA, it must be possible to modulate the emission from a gated cathode with a low-power input signal. This section will discuss a number of important factors that influence the suitability of a gated cathode for high-frequency modulation. The requirements for tube operation, the physical and practical considerations that limit the emission current, the beam quality that can be achieved with such emitters, and the reliability of such emitters will be discussed.

Transit Time. The performance of a gated cathode will degrade if the RF fields experienced by an electron change appreciably during its transit from the emitting surface to the gate–anode region. In a gridded thermionic cathode, the dc bias voltage on the grid is usually negative with respect to the cathode in order to suppress the extraction of thermally emitted electrons by the anode electric field. The grid rarely has positive polarity because it will then intercept emitted current, which would unacceptably load the input circuit and damage the grid at high power densities. Consequently, the electric field that accelerates electrons away from a thermionic cathode is relatively small, and in fact must be negative for part of each RF cycle in Class-C operation. In contrast, the strong electric fields at the emitting surface of a FEA accelerate emitted electrons to high velocity immediately upon emission. Because the gate electrode is approximately coplanar with the emitting tip, the electron passes from the influence of the oscillating gate potential into that of the anode static field in a short distance. In this context, "transit time" refers to the time that an electron spends under the influence of the electric field between the cathode and gating structure. In gridded thermionic cathodes, it is the time for an electron to reach the plane of the grid, while in FEAs it is the time for an electron to reach the gate potential.

Emission-gated cathodes offer the most dramatic performance advantages in Class-C operation. Under these conditions, an accurate determination of the limitations imposed by transit-time effects requires simulations of two-dimensional electron trajectories that include time-varying space charge and electrons that return to the emitting surface. However, transit-time effects in thermionic and field-emission cathodes can be roughly compared by focusing on the gross distinctions between the two structures. The gate voltage of a field emitter, V_G, modulates the current by causing electron emission, while the grid voltage of a thermionic emitter, V_{gr}, modulates the current by suppressing electron extraction from the thermally emitted cloud on the cathode surface. For a space-charge-limited thermionic cathode with an ideal grid (an ideal grid is a thin, perfectly conducting sheet that intercepts no current), the extracted current is determined by the Child–Langmuir law (53,54),

$$J_{CL} = \frac{4\epsilon_0}{9}\left(\frac{2e}{m}\right)^{1/2}\frac{V_{gr}^{3/2}}{d^2} \tag{7}$$

Consequently, the ratio of the full-on voltage V^+_{gr} to cutoff voltage V^-_{gr} required for a ratio of full-on current I^+ to cutoff current I^- of $I^+/I^- = 1000$ is

$$\frac{V_{gr}^+}{V_{gr}^-} = \left(\frac{I^+}{I^-}\right)^{2/3} = 100 \tag{8}$$

Thus, the ratio of the maximum to the minimum electric field that accelerates electrons away from the cathode is 100. The electrons emitted near cutoff depart the cathode surface with only 1% of the acceleration of electrons emitted near full-on conditions.

In contrast, for a field emitter the current is given by (Eq. 3), and the ratio of the currents is

$$\frac{I^+}{I^-} = \left(\frac{V_G^+}{V_G^-}\right)^2 \exp\left[-\frac{B}{V_G^+}\left(1 - \frac{V_G^+}{V_G^-}\right)\right] \qquad (9)$$

For $B = 750$ and $V^+{}_G = 75$ V, reasonable values for today's field emitters, (Eq. 9) yields $V^+{}_G/V^-{}_G = 1.6$. The field that accelerates electrons that are emitted near cutoff is over 60% of that at full-on conditions. This simple example shows why field emission is inherently better adapted to Class-C amplifiers than thermionic emission; no field-emitted electron can linger in the time-varying electric field of the gate.

In addition to the differing cutoff conditions of thermionic and field-emission cathodes, the transit time under full-on conditions differs substantially as well. The field between the gate (grid) and the emitting surface can be approximated as a constant equal to the potential change divided by the gate (grid)–cathode distance. For the thermionic cathode, the electric field in the cathode-to-grid region is sufficient to extract the required current density, as determined by the Child–Langmuir law of (Eq. 7). Using $E = V_{gr}/d$ and solving for E gives

$$E = \left[\left(\frac{9}{4}\frac{J_{CL}}{\epsilon_0}\right)^2 \frac{dm}{2e}\right]^{1/3} \qquad (10)$$

For a current density of 2 A/cm^2 and cathode-to-grid separation d of 250 μm, $E = 2.64$ kV/cm, the transit time τ is

$$\tau = \int_0^d \frac{dz}{v(z)} = \sqrt{\frac{m}{2e}} \int_0^d \frac{dz}{\sqrt{\phi(z)}} = \sqrt{\frac{2dm}{eE}} = 100\,\text{ps} \qquad (11)$$

This corresponds to a cutoff frequency $f_c = 1/2\pi\tau \cong 1.6$ GHz. As the gate voltage declines toward cutoff, the transit time approaches infinity, resulting in the return of some electrons to the cathode.

The potential on the axis of symmetry for a gated field emitter with an anode has been derived by Jensen (55):

$$V(z) = V_G \frac{E_T z}{V_G + E_T z}\left(1 + \frac{E_0 z}{V_G}\right) \qquad (12)$$

In (Eq. 12), E_T is the field at the emitter tip on its center axis and E_0 is the background field due to the anode. An emitted electron can be significantly influenced by the gate when $V(z) < V_G$. Solving (Eq. 12) for $V(z) = V_G$ yields an upper bound to the extent of the control region, $z_G = V_G/\ 1/\sqrt{E_T E_0}$. Since collisions can be neglected, the electron velocity $v(z)$ is determined by the electrostatic potential $f(z)$ as

$$\frac{1}{2}mv^2(z) = ef(z) = eV_G \frac{E_T z}{V_G + E_T z}\left(1 + \frac{E_0 z}{V_G}\right) \qquad (13)$$

The electron velocity is

$$v(z) = \sqrt{\frac{2eV_G}{m}}\sqrt{\frac{E_T z}{V_G + E_T z}\left(1 + \frac{E_0 z}{V_G}\right)} \qquad (14)$$

Then, the transit time is

$$\tau = \int_0^{Z_G} \frac{dz}{v(z)} = \sqrt{\frac{mV_G}{2eE_TE_0}} \int_0^1 \sqrt{\frac{u + \sqrt{E_0/E_T}}{u(1 + \sqrt{E_0/E_T}u)}} du \cong \sqrt{\frac{mV_G}{2eE_TE_0}} \tag{15}$$

In (Eq. 15),$\sqrt{E_0/E_T}$ has been used in approximating the integral. In a nominal FEA, a gate voltage of 75 V produces a tip field of 0.5 V/Å. The anode field must be large enough to draw all of the field-emitted current away from the grid, yet small enough to avoid are breakdown. A value of 20 kV/cm is reasonable for moderate emission currents; this is much higher than for thermionic emission because of the very high local current densities obtained from field emitter arrays. The transit time is then $\tau = 0.15$ ps, which is nearly three orders of magnitude shorter than the thermionic case and corresponds to $f_c \cong 1000$ GHz.

Input Impedance. Although the transit time is diminished by the close spacing of the gate and cathode, the grid–cathode capacitance is increased. Further, the gate–cathode region constitutes a distributed transmission line, as depicted in Fig. 7 Calame (56) has provided a detailed analysis of the voltage distribution within the FEA and the input impedance presented by the FEA. A simplified version is given here.

The array is assumed to be comprised of cells that repeat with periodicity a. The gate capacitance of each repeat cell arises from the capacitance through the gate insulator, C_{pc}, and the gate–tip capacitance C_{tc}, as shown in Fig. 7(a). If the extent of the array in the direction of propagation (the z direction, hereafter called the length) is l and the array width is w, the capacitance per unit length, C, is

$$C = \frac{w\,(C_{tc} + C_{pc})}{a^2} \tag{16}$$

If the effects of the gate–tip holes are neglected (Calame includes these effects and shows them to be small), the resistance per unit length is $R = \rho_G/wt$, where ρ_G and t are the resistivity and thickness of the gate metal, respectively. Using a transverse electric magnetic (*TEM*) transmission-line approximation (57), the inductance per unit length is $L = \mu_0\, h/w$, where μ_0 is the permeability of free space and h is the gate–insulator thickness.

The RF gate voltage $V^{RF}{}_G\,(z, t) = \mathrm{Re}[\, V^{RF}{}_G\,(z)\, e^{\omega t}\,]$ and gate current $I^{RF}{}_G\,(z, t) = \mathrm{Re}[\, I^{RF}{}_G(z) e^{j\omega t}\,]$ on the equivalent transmission line of Fig. 7(b) are determined by the transmission-line equations

$$\frac{\partial \tilde{I}_G^{RF}(z)}{\partial_z} = j\omega C \tilde{V}_G^{RF}(z)$$
$$\frac{\partial \tilde{V}_G^{RF}(z)}{\partial_z} = -(R + j\omega l)\tilde{I}_G^{RF}(z) \tag{17}$$

Solving Eqs. (17) subject to the boundary condition that an open circuit exists at $z = 0$ [$\tilde{I}^{RF}{}_G\,(0) = 0$] gives

$$\tilde{V}_G^{RF}(z) = V_0 \cos(\beta z)$$
$$\tilde{I}_G^{RF}(z) = \frac{V_0}{jZ_0} \sin(\beta z) \tag{18}$$

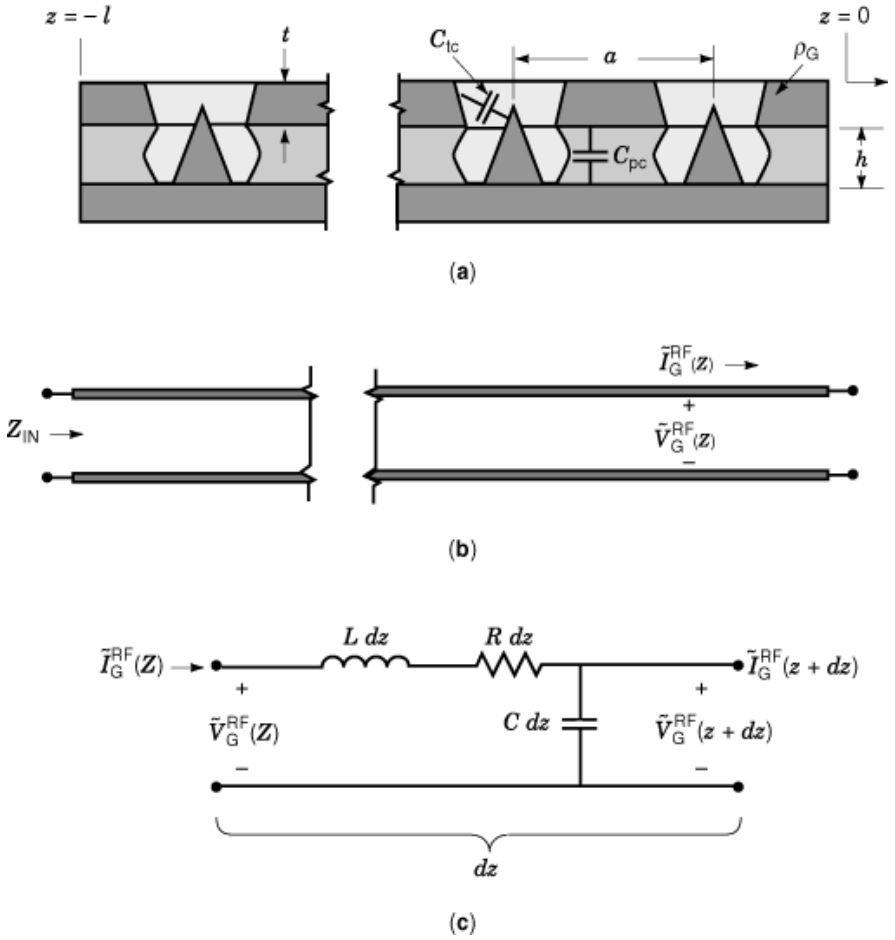

Fig. 7. Transmission-line effects for a gated field-emitter array. (a) The relevant parameters of a gated FEA input circuit. (b) The equivalent transmission line. (c) The incremental transmission line used to calculate the gate-voltage distribution.

where

$$\beta = \omega\sqrt{LC}\left(1 - j\frac{R}{\omega L}\right)^{1/2}$$
$$= \frac{\omega}{a}\sqrt{\mu_0 h\,(C_{pc} + C_{tc})}\left(1 - \frac{j}{\omega}\frac{\rho_G}{\mu_0 h}\right)^{1/2}$$
$$Z_0 = \sqrt{\frac{L}{C}}\left(1 - j\frac{R}{\omega L}\right)^{1/2}$$
$$= \frac{a}{w}\sqrt{\frac{\mu_0 h}{C_{pc} + C_{tc}}}\left(1 - \frac{j}{\omega}\frac{\rho_G}{\mu_0 h}\right)^{1/2}$$

Thus, the gate input impedance Z_{in} is

$$Z_{\text{in}} = \frac{\tilde{V}_{\text{G}}^{\text{RF}}(-l)}{\tilde{I}_{\text{G}}^{\text{RF}}(-l)} = -jZ_0 \cot(\beta l) \tag{19}$$

Fr $\beta\, l \ll 1$, the cotangent function can be expanded, and

$$\begin{aligned} Z_{\text{in}} &= \frac{Rl}{3} + \frac{1}{j\omega(Cl)} + j\omega\frac{Ll}{3} \\ &= \frac{\rho_{\text{G}}}{3t}\frac{l}{w} + \frac{1}{j\omega N_{\text{T}}\left(C_{\text{tc}} + C_{\text{pc}}\right)} + j\omega\frac{\mu_0 h}{3}\frac{l}{w} \end{aligned} \tag{20}$$

The quantity N_{T} is the total number of tips in the array.

Equation (18) shows that each tip does not experience the same gate–tip voltage. To examine the consequences of the gate voltage distribution upon the emission current, assume that the current emitted per tip, $I_{\text{T}}\ (z)$, is proportional to the gate voltage, that is, $I_{\text{T}}\ (z) = g_{\text{mT}}\ V_{\text{G}}\ (z)$. The parameter g_{mT} is thus the transconductance per tip. The current emitted per unit length, $K_{\text{B}}(z)$, is then given by

$$K_{\text{B}}(z) = \frac{w}{a^2} I_{\text{T}}(z) = \frac{w}{a^2} g_{\text{mT}} V_{\text{G}}(z) \tag{21}$$

The total emission current I_{B} is

$$I_{\text{B}} = \int_{-l}^{0} K_{\text{B}}(x)dx = \frac{w g_{\text{mT}}}{a^2}\int_{-l}^{0} V_{\text{G}}(x)dx = N_{\text{T}} g_{\text{mT}} \frac{\sin(\beta l)}{\beta l} \tag{22}$$

Thus, the reduction of the transconductance by nonuniform gate voltage is expressed by the term sin $(\beta l)/\beta l$, implying that the entire array will not be effectively modulated unless $|\beta l| \ll 1$.

The small dimensions of a FEA, together with the high emission current required by a microwave tube often result in input impedance much lower than 50 Ω. Within a factor of 2, the total capacitance per cell, $C = C_{pc} + C_{\text{tc}}$, may be estimated as the parallel-plate capacitance $C = \epsilon a^2/h$. Suppose that a total emission current of 100 mA is required from a FEA for which $A = 1\ \mu$m, $h = 1\ \mu$m, and $I_{\text{T}} = 1\ \mu$A. Neglecting resistive losses, $\beta = 4.2\ \text{cm}^{-1}$, which implies that l must be less than 250 μm for $\beta\, l < 0.1$. In order to emit 100 mA at 1 μA/tip, $N_{\text{T}} = 10^5$ tips must be used. For $l = 250\ \mu$m, $w = N_{\text{T}}\ a^2/\ l = 400\ \mu$m. Using (Eq. (19)), the input reactance is then approximately 5 Ω at 10 GHz. Consequently, an impedance-matching network must be inserted between the power source and FEA to efficiently couple the power to the FEA, as shown in Fig. 8(a)

Impedance-matching considerations are important because they can affect the FEA design and packaging techniques. In the equivalent circuit on Fig. 8(b), the FEA is represented by a series connection of a resistor r_{L} and capacitor c_{L}, and the source is represented by a source conductance $g_{\text{S}} = 1/\ r_{\text{S}}$. By Poynting's theorem (58), the input admittance of the matching circuit, Y_1, is given by

$$Y_1 = \frac{2P_{\text{d}} + 4j\omega(\langle W_{\text{e}}\rangle - \langle W_{\text{m}}\rangle)}{|\tilde{V}_1^{\text{RF}}|^2} \tag{23}$$

In (Eq. (23)), P_{d} is the power dissipation and $\langle W_{\text{m}}\rangle$ and $\langle W_{\text{e}}\rangle$ are the average magnetic and electric energies, respectively. For optimum power transfer, $Y_1 = g_{\text{S}}$, so that $\langle W_{\text{m}}\rangle = \langle W_{\text{e}}\rangle$, that is, the circuit is resonant. For

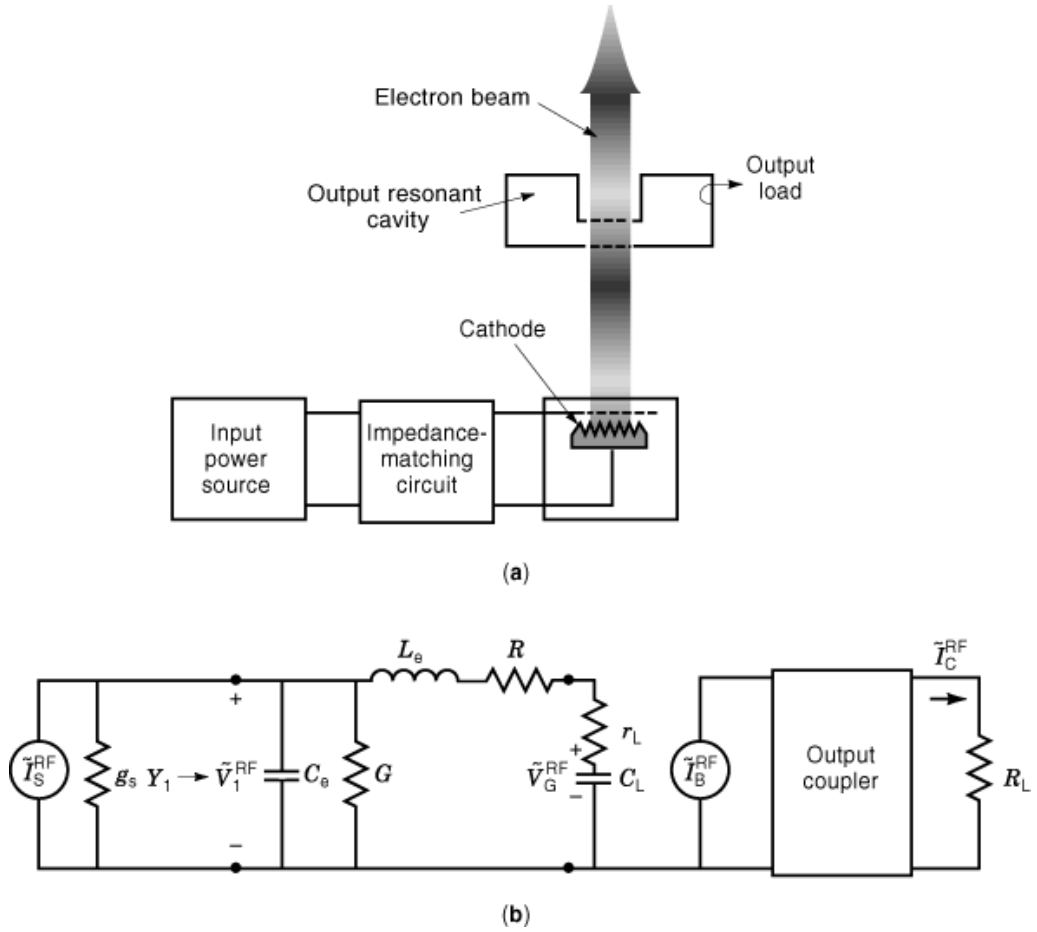

Fig. 8. Input circuit of a field-emitter array. (a) A power source is coupled to the gate of an FEA by an impedance-matching network. (b) An equivalent circuit for the input networks. The impedance-matching network is a resonant circuit that is resonant at the operating frequency. The resonant circuit is characterized by circuit elements C_e, G, L_e, and R .

a frequency near the resonant frequency, the circuit can be approximated by an effective inductance L_e and capacitance C_e as shown in Fig. 8(b). The values of C_e and L_e are chosen so that resonance obtains at the design frequency ω, presenting a parallel resonance at port 1 and a series resonance at port 2. A parallel conductance G and a series resistance R are added to C_e and L_e, respectively, to represent losses in the matching circuit. For simplicity, it will be assumed that

$$\frac{\omega L_e}{R} = \frac{\omega C_e}{G} = Q \tag{24}$$

The quantity Q is the quality factor of the matching circuit. Circuit analysis yields the ratio of the RF output power $P^{RF}{}_O$ to the RF power available from the source, $P^{RF}{}_A$,

$$\frac{P_O^{RF}}{P_A^{RF}} = \frac{4r_L g_S}{\left[1 - \chi_c + (g_S + G)\right]^2 + \chi_c \left(\frac{(r_L + R)}{\eta} + \eta(g_S + G)\right)^2} \tag{25}$$

In (Eq. (25)),

$$\chi_c = \omega^2 L_e C_e \left(1 - \frac{1}{\omega^2 L_e c_L}\right)$$
$$\eta = \sqrt{\frac{L_e}{C_e}\left(1 - \frac{1}{\omega^2 L_e c_L}\right)} \tag{26}$$

The maximum value of $P^{RF}{}_O$ as a function of ωL_e is

$$\left(\frac{P_O}{P_A}\right)_{max} = \left(\frac{r_L}{r_L + R}\right)\left(\frac{g_S}{g_S + G}\right) \tag{27}$$

and occurs when

$$\omega L_e = \sqrt{\frac{r_L + R}{g_S + G}}\sqrt{1 - (r_L + R)(g_S + G)}$$
$$+\frac{1}{\omega c_L} \cong \sqrt{\frac{r_L}{g_S}} + \frac{1}{\omega c_L}$$
$$\omega C_e = \sqrt{\frac{g_S + G}{r_L + R}}\sqrt{1 - (r_L + R)(g_S + G)} \cong \sqrt{\frac{g_S}{r_L}}$$

It is clear from (Eq. (27)) that r_L must be much larger than R to avoid power loss by the matching circuit. An estimate of R and G can be obtained by using (Eq. (24)) in (Eq. 27), which gives

$$R = \frac{\omega L_e}{Q} \cong \frac{1}{Q}\left(\sqrt{\frac{r_L}{g_S}} + \frac{1}{\omega c_L}\right)$$
$$G = \frac{\omega C_e}{Q} \cong \frac{1}{Q}\sqrt{\frac{g_S}{r_L}} \tag{28}$$

Defining the load quality factor $Q_L = 1/\omega\, r_L\, c_L$, (Eq. (28)) gives a condition for efficient

$$r_L \gg R \cong \frac{1}{Q}\left(\sqrt{r_L r_S} + \frac{1}{\omega c_L}\right) \quad \text{or} \quad Q \gg \sqrt{\frac{r_S}{r_L}} + Q_L \tag{29}$$

The matching circuit must be designed so that (Eq. 29) is not violated. Alternately, the FEA designer, faced with unavoidable circuit losses, must design both the FEA and the FEA packaging with (Eq. 29) in mind. The matching circuit can be realized in a variety of ways. Stub transmission lines near the emitting area may be used to add the shunt inductance needed to match to the capacitance of the FEA to the input transmission line. For narrow-band operation, a quarter-wave impedance transformer (57) can be used. Lumped-element circuits often are more compact, but suffer from low quality factors.

The emission current is modulated by the RF voltage that is applied to the gate, $\tilde{V}^{\mathrm{RF}}{}_{\mathrm{G}}$, as shown in Fig. 8(b). This voltage is given by

$$\left|\tilde{V}_G^{\mathrm{RF}}\right|^2 = \frac{2P_O^{\mathrm{RF}}}{r_{\mathrm{L}}(\omega c_{\mathrm{L}})^2} = \frac{2_{\mathrm{gS}}P_{\mathrm{A}}^{\mathrm{RF}}}{(\omega c_{\mathrm{L}}(g_{\mathrm{S}}+G)(r_{\mathrm{L}}+R)} \cong \frac{2Q_{\mathrm{L}}}{\omega c_{\mathrm{L}}}P_{\mathrm{A}}^{\mathrm{RF}} \quad (30)$$

As an example, at 10 GHz each quadrant of the Lincoln FEA cathode (33) has an input impedance $Z_{\mathrm{FEA}} = 2.5 - j\,12\ \Omega$ and requires a peak-to-peak voltage of approximately 20 V ($|\ V?^{\mathrm{RF}}{}_{\mathrm{G}}\ | = 10$ V) to modulate the emission current. The required power, assuming lossless matching is

$$P_{\mathrm{A}}^{\mathrm{RF}} = \frac{\omega c_{\mathrm{L}}\left|\tilde{V}_{\mathrm{G}}^{\mathrm{RF}}\right|^2}{2Q_{\mathrm{L}}} = \frac{100}{2\times 12.5\times(12.5/2)} = 0.6\,\mathrm{W}$$

Beam-Current Modulation. In the absence of transit-time delays, the waveform of modulated beam current $I_{\mathrm{B}}(t)$ of a gated cathode is given by substituting the gate voltage $V_{\mathrm{G}}(t)$ into the current–voltage relation of the cathode. In the case of a gated FEA, the voltage modulation is usually sinusoidal, and the current–voltage relation of an FEA is taken to be the Fowler–Nordheim relation of (Eq. 3). Because the characteristic curve is nonlinear, the resulting beam current waveform will include harmonic frequencies. Computer simulations must be used to exactly obtain the emission-current modulation that results from a given gate-voltage modulation. However, an approximate analysis, coupled with (Eq. 30), can be used to estimate the beam-current modulation produced by the FEA. The gate voltage is assumed to be

$$V_{\mathrm{G}}(t) = V_{\mathrm{G}}^{\mathrm{dc}} - V_{\mathrm{G}}^{\mathrm{RF}}\cos(\omega t) \quad (31)$$

Then, defining $\chi = V^{\mathrm{RF}}{}_{\mathrm{G}}/V^{\mathrm{dc}}{}_{\mathrm{G}}$ and using (Eq. 3), the emission current is

$$\begin{aligned} I_{\mathrm{B}}(t) &= A\left[V_{\mathrm{G}}^{\mathrm{dc}} - V_{\mathrm{G}}^{\mathrm{RF}}\cos(\omega t)\right]^2 \exp\left(-\frac{B}{V_{\mathrm{G}}^{\mathrm{dc}} - V_{\mathrm{G}}^{\mathrm{RF}}\cos(\omega t)}\right) \\ &\cong A\left(V_{\mathrm{G}}^{\mathrm{dc}}\right)^2 \exp\left(-\frac{B}{V_{\mathrm{G}}^{\mathrm{dc}}\left[1-\chi\cos(\omega t)\right]}\right) \end{aligned} \quad (32)$$

By Fourier analysis,

$$\frac{1}{1-\chi\cos(\omega t)} \cong 1 + \frac{2\chi}{1+\sqrt{1-\chi^2}}\cos(\omega t) \quad (33)$$

If (Eq. 33) is inserted into (Eq. 32), the emission current can be expressed in terms of the fundamental and harmonic frequencies as

$$I_{\mathrm{B}}(t) \cong A\left(V_{\mathrm{G}}^{\mathrm{dc}}\right)^2\left(I_0(\delta) + 2\sum_{k=1}^{\infty} I_k(\delta)\cos(\omega t)\right) \quad (34)$$

In (Eq. 34)

$$\delta = \frac{2B}{V_G^{dc}\sqrt{1-\chi^2}}\left(\frac{\chi}{1+\sqrt{1-\chi^2}}\right)$$

and I_k (z) is the modified Bessel function of the first kind. The identity

$$e^{z\cos(\theta)} = I_0(z) + 2\sum_{k=1}^{\infty} I_k(z)\cos(k\theta)$$

has been used (59). The appropriate modulation will depend on the application: a frequency multiplier will require a more strongly modulated beam than a linear amplifier. Equation (34) is a good indicator of the fraction of the beam energy that can be converted to electromagnetic energy in the fundamental frequency, provided that the inductive output circuit only extracts power from the beam to the circuit. If the output circuit is lengthened to increase the modulation of the beam before extraction begins, space-charge effects and nonlinear interactions between the beam and the inductive output can result in conversion of power between the harmonics (60,61,62).

Writing $I_B(t) = I^{dc}{}_B + \mathrm{Re}[\tilde{I}^{RF}{}_B\, e^{j\omega t}]$, the dc and RF components of the beam current are given by

$$I_B^{dc} = A\left(V_G^{dc}\right)^2 \exp\left(-\frac{B}{V_G^{dc}\sqrt{1-\chi^2}}\right) I_0(\delta)$$
$$\tilde{I}_B^{RF} \cong 2A\left(V_G^{dc}\right)^2 \exp\left(-\frac{B}{V_G^{dc}\sqrt{1-\chi^2}}\right) I_1(\delta) = 2I_B^{dc}\frac{I_1(\delta)}{I_0(\delta)} \tag{35}$$

The values of χ and δ can be estimated for optimal impedance matching using (Eq. 30).

The transconductance of a voltage-controlled current source is another indicator of the efficiency by which gate-voltage RF modulation is converted to emission-current RF modulation (63). It is defined as the incremental change in beam current divided by the incremental change in gate potential, $g_m = \partial I_B/\partial V_G$. In the absence of transit-time effects, the transconductance is the slope of the characteristic curve I_B (V_G); if the characteristic curve is nonlinear, the transconductance will depend upon V_G. The transconductance of a gated FEA is thus

$$\frac{\partial I_B}{\partial V_G} = AV_G\left(2+\frac{B}{V_G}\right)\exp\left(-\frac{B}{V_G}\right) = \left(2+\frac{B}{V_G}\right)\frac{I_B}{V_G} \tag{36}$$

This transconductance, like the current itself, is exponentially sensitive to the Fowler–Nordheim$B$ parameter. To relate cathode performance to the gain of an IOA, a generalized transconductance α may be defined as the incremental RF current that results for an increment in RF gate-driven power, that is, $\alpha = \partial|\tilde{I}^{RF}{}_B|/\partial P^{RF}{}_G$.

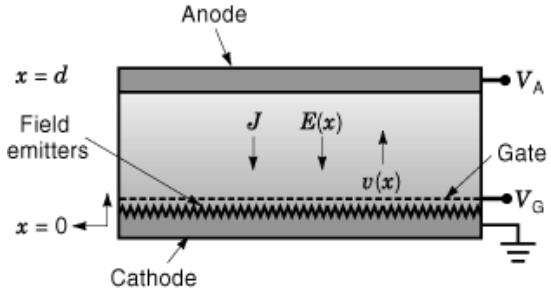

Fig. 9. Simple model used to estimate space-charge effects in a gated field-emitter array cathode.

Since emission gating is performed by applying an oscillating potential to a gate, α is related to g_m as

$$\alpha = \frac{\partial \left| \tilde{I}_B^{RF} \right|}{\partial P_G^{RF}} = \frac{\partial \left| \tilde{I}_B^{RF} \right|}{\partial V_G} \times \frac{\partial V_G}{\partial V_G^{RF}} \times \frac{\partial V_G^{RF}}{\partial P_G^{RF}}$$
$$= g_m \times 1 \times \frac{\partial V_G^{RF}}{\partial P_G^{RF}} = \frac{2Q_L}{\omega c_L} P_A^{RF} g_m \qquad (37)$$

In (Eq. 37), (Eq. 30) has been used to relate ${V^{RF}}_G$ to ${P^{RF}}_A$. This, of course, assumes optimal impedance matching. More generally, the relation between the drive power and the RF voltage at the gate depends upon the input circuit as discussed previously.

Current Density. In most cases, the upper limit to both emission current and current density is posed by reliability considerations. These are discussed later. However, fundamental limits apply to the current that can be obtained from field-emitter cathodes.

Space Charge. As emission current from the cathode increases, the reduction of the field near the cathode by the space charge of the emitted electrons can no longer be neglected. For a FEA diode, the limiting current density is described by the Langmuir–Child law of (Eq. 7) and is determined by the reduction of the extraction field at the tip by the space charge of the emitted electrons (64,65). However, for a gated field emitter, space charge does not greatly diminish the tip field, but rather, gives rise to large gate current. Because of the high current density that is required, such space-charge effects must be considered in any microwave tube design.

The one-dimensional analysis of Lau, Liu, and Parker (66) can be extended to provide some insight into the nature of these effects. A gated FEA with dc voltages V_G and V_A applied to the gate and anode, respectively, is depicted in Fig. 9 To minimize confusion, the polarities of the current density J, electric field $E(x)$ and electron velocity $v(x)$ are defined to be positive for electronic flow from the cathode to the anode. In the gate–anode region ($0 < x < d$), Poisson's equation relates the electrostatic potential $\phi(x)$ to the charge density $\rho(x)$,

$$\frac{d^2\phi(x)}{dx^2} = \frac{\rho(x)}{\epsilon_0} \qquad (38)$$

For static conditions, the current density J is independent of x and is given by

$$J = \rho(x)v(x) \qquad (39)$$

Because field emitters operate in ultrahigh vacuum (*UHV*) conditions, any electronic collisions with gaseous molecules can be neglected, so that $v(x)$ is given by

$$\frac{m}{2}v^2(x) = e\phi(x) \tag{40}$$

The electric field $E(x)$ (using the polarity definitions on Fig. 9) is given as

$$E(x) = \frac{d\phi(x)}{dx} = \frac{m}{e}\frac{dv}{dt} \tag{41}$$

Differentiating (Eq. 41),

$$\frac{d^2\phi}{dx^2} = \frac{m}{e}\frac{d}{dx}\frac{dv}{dt} = \frac{m}{e}\frac{d}{dt}\frac{dv}{dt}\frac{dt}{dx} = \frac{m}{ev}\frac{d^2v}{dt^2} \tag{42}$$

In view of (Eq. 38) and (Eq. 39), (Eq. 42) becomes

$$\frac{d^2v}{dt^2} = \frac{eJ}{\epsilon_0 m} \tag{43}$$

The emitted electrons are assumed incident upon the gate–anode region with a velocity derived from the gate voltage, that is,

$$v(0) = \sqrt{\frac{2eV_G}{m}} \tag{44}$$

Defining $t = 0$ at $x = 0$, and solving (Eq. 43) for $v(t)$ and $x(t)$,

$$\begin{aligned} v(t) &= \frac{eJ}{2m\epsilon_0}t^2 + \frac{eE_S}{m}t + \sqrt{\frac{2eV_G}{m}} \\ x(t) &= \frac{eJ}{6m\epsilon_0}t^3 + \frac{eE_S}{2m}t^2 + \sqrt{\frac{2eV_G}{m}}t \end{aligned} \tag{45}$$

In Eqs. (45), E_S is the electric field at $x = 0$. If the emit- ted electrons reach the anode at time T, Eqs. (45) at $t = T$ become

$$\begin{aligned} \sqrt{\frac{2eV_A}{m}} &= \frac{eJ}{2m\epsilon_0}T^2 + \frac{eE_S}{m}T + \sqrt{\frac{2eV_G}{m}} \\ d &= \frac{eJ}{6m\epsilon_0}T^3 + \frac{eE_S}{2m}T^2 + \sqrt{\frac{2eV_G}{m}}T \end{aligned} \tag{46}$$

In a gated FEA, J is determined by V_G through (Eq. 3) and is thus a given quantity. Thus, Eqs. (46) determine E_S and T as a function of V_G, V_A, J, and d. This allows $x(t)$ and $\phi(t)$ to be determined from Eqs. (40) and (45)

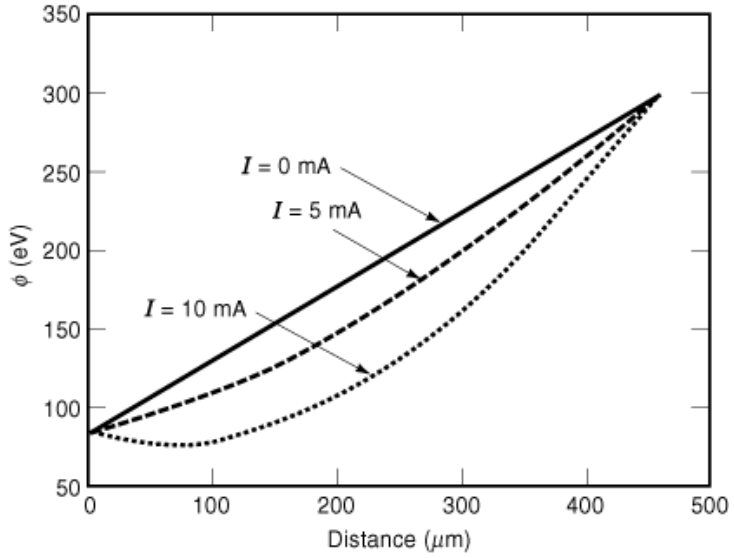

Fig. 10. Calculated dependence of the electrostatic potential in the gate–anode region for several values of emitted current. As the emission current increases, the electric field near the cathode surface diminishes. At sufficiently high emission current, increased gate current results.

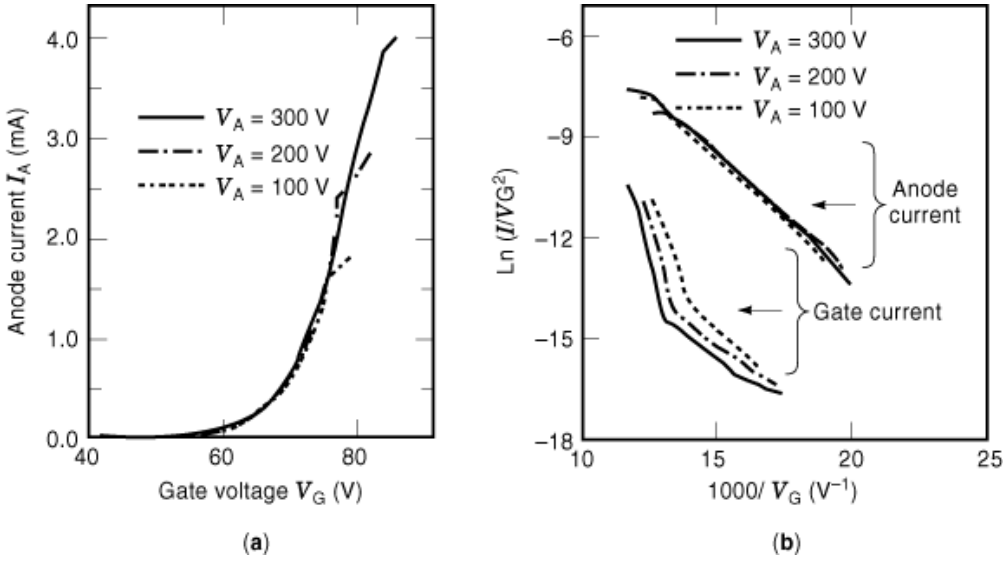

Fig. 11. Experimental manifestation of space-charge effects. (a) Anode current versus gate voltage, showing the saturation of anode current at high emission levels due to the electronic space charge. (b) Fowler–Nordheim plots of gate and anode current, showing the increase of gate current that accompanies anode-current saturation.

Fig. 10 displays the dependence of ϕ upon x for several values of emission current, using the FEA parameters on Fig. 11 later. As J increases, $E_S = d\phi/dx$ diminishes until, analogous to the Child–Langmuir law, $E_S = 0$ at

current density J_L given by

$$J_L = J_{CL}\left(1 - \sqrt{\frac{V_G}{V_A}}\right)\left(1 + 2\sqrt{\frac{V_G}{V_A}}\right)^2 \qquad (47)$$

The quantity J_L only roughly estimates the upper limit to the current density. A number of important factors have been neglected in this simple analysis, including the two-dimensional geometry of the FEA and the spreading of the emitted electron beam. In most cases, numerical simulations (67) must be used to accurately determine these effects. More importantly, the redirection of the emission current from the anode to the gate electrode occurs at current densities lower than J_L. The resulting high gate current degrades FEA performance and enhances failure probability, as discussed laters Fig. 11 shows experimental data from a 6100-tip array that was tested in a UHV probing apparatus (55). The FEA was approximately 25×25 μm^2 in area and the probe anode was spaced about 18 mil from the FEA Fig. 11(a) shows how anode current saturates due to space-charge effects. As the anode voltage is increased, higher values of emitted current can be accommodated, as is indicated by (Eq. 47) Fig. 11(b) shows Fowler–Nordheim plots of the same data and includes the gate current. The departure of the anode current from a Fowler–Nordheim dependence and the accompanying gate-current increase is evident.

Since gain depends so strongly upon minimizing the gate-to-cathode capacitance, a small-area source operating near peak intensity will generally provide the best simultaneous gain and efficiency. As efficiency is also improved by passing the bulk of the beam as close as is practical to the output circuit electrodes, the optimum electron beam geometry is a thin annulus. Because such high-perveance annular beams improve the performance of RF output couplers, it is advantageous to draw the maximum current density consistent with a reasonable cathode lifetime. This raises issues in electron gun design, including initial velocity effects, beam spreading, axial demodulation, beam stability, and perveance enhancement. All are of concern in a design context. Electron guns for inductive output amplifiers should be designed to exploit cathodes such as FEAs that are capable of emitting hundreds of amperes per square centimeter.

Beam Quality. Microelectronic FEAs emit current from sharply pointed cones or pyramids. Although the emitting tips are sharp, the radius of curvature is finite, typically ranging from 10 nm to 100 nm. Electrons are emitted from the sides as well as the tops of the emitter tips, resulting in an angular distribution of the emitted current. Jensen et al. (68) has applied the Fowler–Nordheim equation for the current density to a field emitter that is approximated by hyperbolic surfaces and surrounded by a coplanar anode, as shown in Fig. 12. The electron distribution as a function of emission angle θ_G was calculated, and the rms average angle of emission from a single tip, θ_{rms}, was found to be approximated by

$$\theta_{rms} \equiv \sqrt{\langle \theta_G^2 \rangle} = \sqrt{\frac{1}{2}\left(1 - \frac{I_1(\chi_G)}{I_0(\chi_G)}\right)} \qquad (48)$$

In (Eq. 48), $I_0(x)$ and $I_1(x)$ are modified Bessel functions of the first kind, B and V_G are defined by (Eq. 3), α is the half-angle of the conical emitter tips, and

$$\chi_G = 1 + \frac{B}{2V_G} + \frac{1}{2}\sin^2\alpha \qquad (49)$$

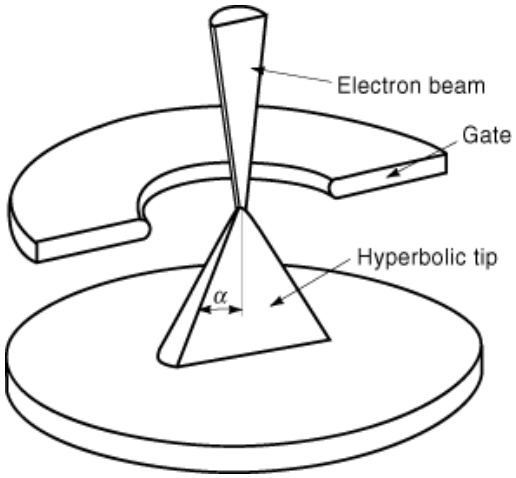

Fig. 12. Field emitter modeled using the surfaces of a hyperbolic coordinate system. Both calculations and experiments show that the angular spread of the emitted electron beam is approximately 20°.

Experimental measurements of single-tip emitters with $\theta_{\rm rms}$ of 20° correlated well with the theory. The mean transverse energy is given in terms of the emittance and the gate potential by

$$E_{\perp} = eV_{\rm G}\frac{\sin^2\theta_{\rm rms}}{1+\sin^2\theta_{\rm rms}} \qquad (50)$$

Thus for example, electrons emitted from a tip having a mean angle of emission of 20° have a mean transverse energy of 0.1 $V_{\rm G}$, which implies $E_{\perp} \cong 5$ eV for contemporary submicron FEAs. This transverse energy is irreducibly introduced into the electron beam.

For the linear-beam amplifiers considered here, the angular emission of the FEA is likely to be a serious concern at frequencies above X band. At such short wavelengths, the small size of the output circuit demands a small beam diameter, and low beam voltage is required because small circuits are not able to dissipate as much power. Therefore, for high frequencies, low gate voltages are required to achieve acceptable beam quality as well as to reduce the drive power. For some applications, such as gyroamplifiers and free-electron lasers, maintaining a high-quality beam is of paramount importance. Focusing grids have been suggested as a means of collimating the emission from single tips.

Lifetime and Failure Mechanisms. The greatest limitation to the utility of FEAs in applications requiring high emission currents, such as the microwave tube application, is the precocious and seemingly random failure of the FEAs at high emission currents. The environment and procedures used in testing field emitters have proved to be quite critical. Hydrocarbon-free UHV vacuum, lengthy in situ conditioning procedures, and electrostatic safeguards are necessary to FEA longevity. In ultraclean conditions, several studies of single-tip field emitters have shown that tip failure is predictable and occurs at tip currents in the multimilliamp range (69,70,71,72). For example, resistive heating was identified as the failure mechanism of single-tip emitters fabricated out of single-crystal tungsten (69,70). In this study, repeatable precursors of failure were identified that enabled tips to be reversibly cycled near burnout conditions. Unfortunately, trace amounts of contamination invariably remain because of the fabrication processing of an FEA, and the environment near the FEA cathode in a microwave tube invariably contains absorbed impurities. Fig. 13 shows data taken on Lincoln Laboratory emitters (33). In this case, the conical molybdenum tips were approximately 2000 Å high with a

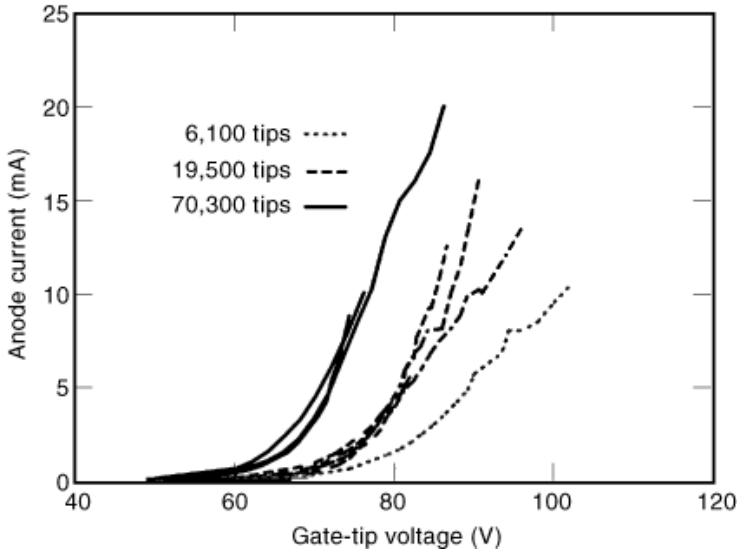

Fig. 13. Tip failure data for Lincoln Laboratory field-emitter arrays. Emission currents exceeding 20 mA and tip currents exceeding 1.7 μA were attained. The incidence of failure does not correlate well with the average current per tip.

conical half angle of 30° and a radius of curvature of approximately 100 Å. Arrays of different size were tested to destruction in a UHV probing station. Assuming a uniform distribution of current across the array, failure occurred for the 6,100-tip array at 1.7 μA/tip, while the best 70,300-tip array failed at 0.3 μA/tip.

A simple analysis can be used to show that these tip currents do not heat the tips to unacceptable temperatures. The tip is approximated by a conical section of a sphere having inner radius a, outer radius b, and conical half angle α. In operation, tip heating arises from two sources. The first of these is resistive heating by the emission current, and the second is Nottingham heating (73). Nottingham heating is described by a thermal heat flux $\varphi_0 = J_T\ (\ E_F - E\ )$ at the emitting surface, where J_T is the tip current density, E_F is the Fermi-level energy, and E is the average energy of the emitter electrons. The energy deposited per emitted electron, $E_d = E_F - E?$ is approximately 0.25 eV (74). If we neglect any angular variations and use spherical coordinates, the tip temperature $T(\ r\ ,\ t)$ is given by the equation (75)

$$\frac{1}{\kappa}\frac{\partial T(r,t)}{\partial t} = \frac{1}{r^2}\frac{\partial}{\partial r}\left(r^2\frac{\partial T(r,t)}{\partial r}\right) + \frac{A(r)}{K_{th}} \qquad (51)$$

In (Eq. 51), $\kappa = K_{th}/\rho_m\, c_p$, and K_{th}, ρ_m and c_p are the tip– metal thermal conductivity, mass density, and specific heat, respectively. If I_T is the tip current and ρ_e is the electrical resistivity of the tip metal, the resistive power dissipation $A(\ r\ )$ is

$$A(r) = \rho_e\left(\frac{I_T}{2\pi(1-\cos\alpha)r^2}\right)^2 \qquad (52)$$

The thermal boundary conditions are that a thermal flux φ_0 is applied at $r = a$, and that $T = T_0$ at $r = b$. For $A \ll b$, the steady-state solution for the tip temperature is

$$T(\alpha) - T_0\,\frac{I_T E_d}{2\pi a(1-\cos\alpha)K_{th}}\left(\frac{\rho_e I_T^2}{\pi a(1-\cos\alpha)} + I_T E_d\right) \qquad (53)$$

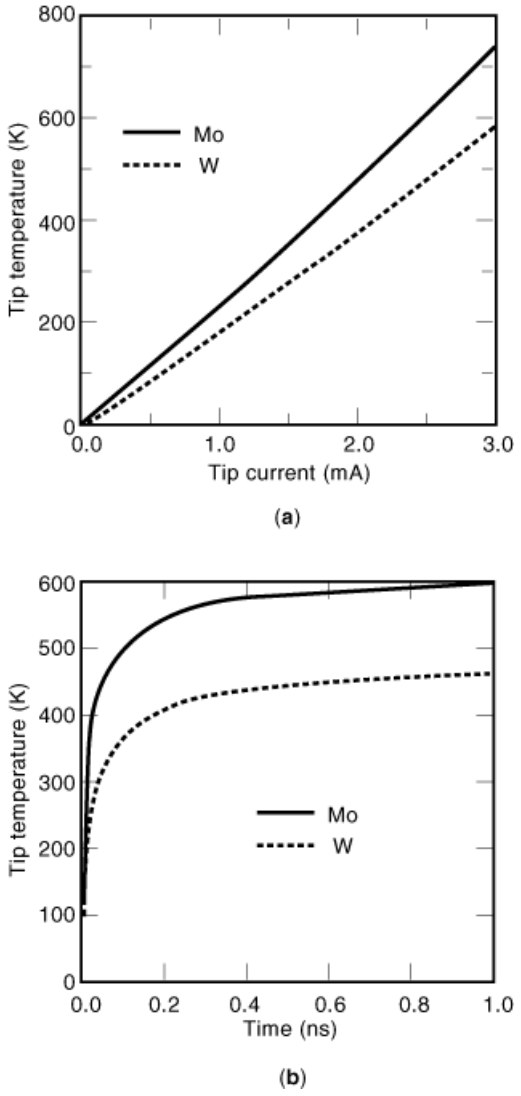

Fig. 14. Calculated tip temperature during emission. A simple analytic model that includes resistive heating and Nottingham heating is used. Si and Mo conical tips are considered, with tip height 2000 Å, tip radius 100 Å, and conical half angle 30°. (a) Steady-state temperature (tip heating) versus tip current. (b) Transient temperature response for an initial tip-current step of 3 mA.

If resistive heating is neglected, the transient temperature response is

$$T(a,t) - T_0 = \frac{I_T E_d}{2\pi a(1-\cos\alpha)K_{th}}\left[1 - e^{\kappa t/a^2}\operatorname{erfc}\left(\frac{\sqrt{\kappa t}}{a}\right)\right] \tag{54}$$

The tip temperatures predicted by (Eq. 2) for molybdenum and silicon tips are plotted in Fig. 14 Only modest temperatures are predicted for the average tip currents on Fig. 13 Ancona (76,77), using detailed simulations,

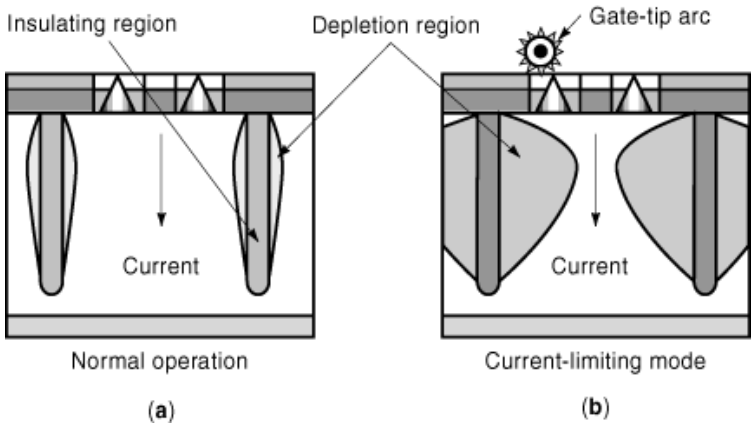

Fig. 15. Schematic diagram of VECTL-stabilized field-emitter array. An arc causes the tip potential to rise to the gate-voltage level. Depletion regions (shaded) are induced by the increased bias across the VECTL channel, which increases the resistance of the VECTL structure thereby limiting emission current. (a) Normal opera- tion. The VECTL structure presents a low series resistance. (b) Response to an event that would increase the tip current. The VECTL channel constricts, presenting high impedance that limits current flow.

also concludes that experimentally observed FEA failures cannot be explained by tip heating if a uniform distribution of tip currents across the array is assumed.

Equation (53) however, does predict that the tip temperature would be much higher if the emission current of the array were concentrated in one or several tips. This is quite possible because of imperfections in the FEA fabrication process. Furthermore, as suggested by Charbonnier (74) and Fursey (71,72) random processes associated with migration of surface contaminants or changes in surface morphology could give rise to tip-destroying bursts of emission or gate current. This also is quite plausible since the thermal time constants predicted by Eq. (Eq. 54) imply that a large excursion in tip temperature will result from short ($\sim$1 ns) current pulses.

Current limiting by external circuit elements has proved effective in reducing tip burn out. The simplest such scheme, which is used in field emitters for display applications, is to incorporate a resistor in series with the tips (8,78). Because of such resistive stabilization, cathode arcing is no longer considered an issue for displays and lifetimes exceeding 1000 hours are routinely achieved. However, any resistance that is introduced into the FEA equivalent circuit could limit the ability to modulate the emission at GHz frequencies. Recently, NEC Corporation has described the vertical current limiter (*VECTL*) approach (17,18,19), which has enabled much higher currents, stability, and longevity in a tube environment. In the VECTL scheme, depicted in Fig. 15 the pinch-off of a field-emission-transistor–like structure beneath the emitters limits the current, thereby preventing any dramatic rises in current. Under conditions of an arc, the bias across the VECTL channels substantially increases, which causes the conducting channel to constrict. This greatly increases the effective resistance and limits the current. In normal operation, the resistance of the VECTL structure had a negligible effect on the current. Stable pulsed dc emission at current levels sufficient for meaningful levels of gain and power output was obtained for 5000 h without FEA failure, an unprecedented achievement.

The current-limiting structures just described do not address the fundamental causes of tip failure. These causes are quite diverse and include poor vacuum, improper anode design, surface flashover (79) of the gate insulator, contamination, and surface irregularities. It is likely that the elimination of the causes of failure will involve stringent cleaning procedures and/or the use of ultraclean and stable tip materials. Both approaches have been used, but often the only effective cleaning procedure involves high-temperature bake outs that are impractical for many applications. A number of new materials for tips are under development that promise

to improve upon the characteristics of molybdenum, silicon, or tungsten tips. Encouraging results have been obtained from carbide (80,81,82) and nitride (83,84) field emitters.

Characteristics of FEA–Cathode Microwave Tubes

When a gated cathode is used to modulate the electron beam, the function of the output circuit is to couple RF power from the beam to an electromagnetic wave. The choice of output circuit, whether cavity, coupled cavity, ring bar, or helix, will depend chiefly on the bandwidth, the size, and the output power required of the amplifier. The modulated current [see (Eq. 34)] that is available from the gated FEA cathode also influences the choice of circuit.

Efficiency. Intuitively, one might expect that a more strongly modulated beam would result in superior efficiency, but this is not always the case. In a broad-band output circuit, a strongly modulated beam can drive higher-frequency parasitic modes that reduce the efficiency. In a narrow-band output circuit, any high-frequency modes on a strongly modulated beam pass through the circuit without exciting parasitic modes. However, the high-frequency modes increase the peak electric field in the gap, which limits the power handling capability of the output cavity. In addition, strong modulation severely reduces the gain, which must be included in any performance optimization.

To optimize the tube for total efficiency, both the beam power converted to RF and the beam power recovered in the collector must be considered. The total beam power P_b entering the tube leaves as output power P_o, as power recovered in the collector P_C, and as waste heat in the collector. The net efficiency of the amplifier, η_N, is given by

$$\eta_N = \frac{\eta_e}{1 - \eta_C (1 - \eta_e)} \tag{55}$$

In (Eq. 55), $\eta_e = P_o/P_b$ is the electronic efficiency, and $\eta_C = P_C /(P_b - P_o)$ is the collector efficiency. The collector efficiency depends upon both on the "quality" of the spent beam and the design of the collector itself. If the spent beam enters the collector with a broadly smeared velocity distribution, much less energy will be recovered than if the decelerated electrons have nearly the same energy. Therefore, in optimizing an output coupler for an IOA, equal attention must be given to the RF power that is coupled out and the velocity distribution of the spent beam.

Klystrode Output Power. A klystrode extracts RF power from the beam by passing the beam through a capacitive gap in a resonant cavity, as illustrated in Fig. 2 The operation of a klystrode output cavity is fundamentally similar to the final cavity of a klystron. The constraints are the same, with the exception that the quality factor of the output cavity Q must be appropriate to the current ratio of the injected beam.

According to a theorem first derived by Shockley (85), the current induced in the plates of a capacitive gap by an electron beam having a current $I_B(x,t)$ is

$$I_c(t) = \frac{1}{d} \int_0^d I_B(x,t) dx \tag{56}$$

In (Eq. 56), the capacitive gap extends from $x = 0$ to $x = d$. In operation, the modulated electron beam that is incident upon the cavity induces a RF current at the input terminals of the output cavity according to (Eq. 56). Since the klystrode operates at the resonant frequency of the cavity, the cavity presents high resistance R_c at the operating frequency and presents much lower impedance at other frequencies. Consequently, a RF voltage $V^{RF}{}_c(t) = \mathrm{Re}\ (V?^{RF}{}_c\ e^{j\omega t})$ is developed across the gap that, together with the electronic space charge,

modifies the electrostatic potential and electron velocity within the gap. The power available from a cavity output circuit is obtained from the conservation of energy (86):

$$\frac{dW}{dt} = -\frac{\omega_0}{Q}W + \langle E \cdot J \rangle \tag{57}$$

The maximum energy in the cavity is limited by arcing in regions of strong electric field, usually in the cavity gap near the beam. The rate of power extraction from the beam $\langle E \cdot J \rangle$ is limited by the deceleration of the electrons by the electric fields induced in the coupling gap. The harmonic content of the beam current and the Q of the cavity determine the harmonic content of $\langle E \cdot J \rangle$. This is often an important design factor. Higher-order harmonics contribute no usable output power, but increase the electric field in the cavity, reducing the maximum output power.

The interaction between electron beam and the output cavity is quite complex and can only be treated accurately using computer-aided techniques. However, a simple analysis can display some important characteristics of the output coupling. As the beam enters the gap, at $x = 0$, the beam current can be written as

$$I_B(0,t) = I_B^{dc} + \mathrm{Re}\left(\tilde{I}_B^{RF} e^{j\omega}\right) \tag{58}$$

In (Eq. 58), $I^{dc}{}_B$ is the dc component of the electron beam and $\tilde{I}^{RF}{}_B$ is a complex quantity that describes the emission-current modulation at the RF frequency ω. The electronic charge density in the absence of electric field in the coupling gap, $\rho^0{}_B\,(x,t)$ is given by the current-continuity equation as

$$\rho_B^0(x,t) = \frac{\tilde{I}_B^{dc}}{v_0 A} + \mathrm{Re}\left(\frac{\tilde{I}_B^{RF}}{v_0 A} e^{-j\omega x/v_0} e^{j\omega x}\right) \tag{59}$$

The velocity of the electrons, $v_e(x,t)$, is determined by the electric field within the gap and the anode voltage V_A according to

$$\frac{m}{2} v_e^2\,(x,t) = eV_A + e\phi(x,t) \tag{60}$$

If space-charge effects are neglected, and $|V_c(t)| \ll V_A$,

$$v_e(x,t) = v_0\sqrt{1 + \frac{\phi(x,t)}{V_A}} \cong v_0 + \frac{v_0}{2V_A}\phi(x,t) \cong v_0 + \frac{v_0 x}{2V_A d}V_c(t) \tag{61}$$

In (Eq. 61), $v_0 = \bar{I}$ is the velocity of the electrons at $x = 0$ as they enter the coupling gap. If the RF modulation of the electron beam is small compared to the dc current, the induced current can be approximated, using

(Eq. 56), as

$$I_c\,(t) = \frac{A}{d}\int_0^d \rho(x,t)v(x,t)dx$$
$$\cong \int_0^d \left\{ \frac{I_B^{dc}}{d} + \mathrm{Re}\left[\left(\frac{\tilde{I}_B^{RF}}{d} e^{-j\omega x/v_0} + \frac{I_B^{dc} x}{2V_A d^2} \tilde{V}_c \right) e^{j\omega t} \right] \right\} dx \tag{62}$$

If the induced current is described by $I_c\,(t) = I^{dc}{}_c + \mathrm{Re}\,(\tilde{I}^{RF}{}_c\, e^{j\omega t}\,)$, (Eq. 62) gives

$$\tilde{I}_c^{RF} = \tilde{I}_B^{RF} e^{-j\omega d/2vo} \left(\frac{\sin(\omega d/2v_o)}{\omega d/2v_o} \right) + \frac{\tilde{I}_B^{dc}}{4V_A} \tilde{V}_c^{RF} \tag{63}$$

Using $V^{\sim} = \mathrm{R}\, I^{\sim RF}{}_c$ in (Eq. 63) and solving for $I^{\sim RF}{}_c$,

$$\tilde{I}_c^{RF} \cong \frac{\frac{\sin(\omega d/2v_0)}{\omega d/2v_0}}{1 + \frac{R_c|I_B^{dc}|}{4V_A}} \tilde{I}_B^{RF} \tag{64}$$

The RF output power $P^{RF}{}_O$ then is

$$P_0^{RF} = \frac{R_c}{2}\left|\tilde{I}_c^{RF}\right|^2 = \frac{R_c}{2} \frac{\left(\frac{(\sin(\omega d/2v_0)}{\omega d/2v_0} \right)^2}{\left(1 + \frac{R_c|I_B^{dc}|}{4V_A} \right)^2} \left|\tilde{I}_B^{RF}\right|^2 \tag{65}$$

(Eq. 65) shows that the quantity $\omega\, d/2v_0$ must be small for efficient operation.

Consequently, the output cavity must be designed so that $d \ll (1/\pi f)\sqrt{2eV_A/m}$. At $f = 10$ GHz with $V_A =$ 5 kV, this implies that $d \ll 1$ mm. Equation (65) also shows the first-order effects of the deceleration of the electron beam by the RF voltage and indicates that there are design tradeoffs involving the beam modulation, output-cavity quality factor, and anode voltage.

Output circuit efficiency for the klystrode can be predicted using techniques ranging from basic analytical theory to detailed electromagnetic particle-in-cell (*PIC*) simulation. Resonator saturation theory (*RST*) (86) is an analytical approach that predicts the power in the output cavity from startup through saturation. It is based upon the conservation of energy, (Eq. 57); the power loss term $\langle E{\cdot}J \rangle$ is calculated by integrating the electron velocities crossing the gap with sinusoidal voltage. For simple assumptions, an analytical result can be obtained; otherwise, the power-loss term must be integrated numerically. In this manner, details such as arbitrary bunch and interaction field shape can be included.

When space charge is important one can resort to multidimensional, electromagnetic PIC techniques such as MAGIC (87) to obtain a fully self-consistent calculation of the beam interaction with the circuit. In the PIC code, the circuit can be modeled with a full-cavity transient simulation or with a *port approximation*—a transmission line. The predictive accuracy of these methods has been well substantiated, most notably for the

487 MHz klystrode design by Varian, for which the code predicted 71% efficiency in excellent agreement with the experimental data (88).

The Klystrode designed by workers at Communications and Power Industries (*CPI*) is intended to provide an output power of 50 W at 10 GHz using a gated FEA cathode. It requires a peak current of 112 mA from a ring cathode with inner and outer diameters of 550 μm and 610 μm, respectively (89). Twystrodes, investigated at the Naval Research Laboratory (90), require similar (but potentially higher) currents. For example, if a gate voltage $V_G(t) = V_{pk} - V_{RF}\,[1 - \cos(\omega t)\,]$ is applied to a reduced-geometry FEA as described before, $V_{pk} = 39.3$ V and $V_{RF} = 11.9$ V will produce the required $I_{ave}/I_{pk} = 0.2$ and correspond to a peak current density of 100 A/cm^2. In separate measurements of field emitters, currents of 180 mA have been obtained, and current densities in excess of 2000 A/cm^2 have been obtained by Stanford Research Institute (*SRI*) and Massachusetts Institute of Technology Lincoln Laboratory. Emission currents as high as 22 mA/quadrant have been obtained in test stations for four-quadrant ring cathodes (33), but only 2.6 mA/quadrant has been obtained in the klystrode vehicle. In the tube, cathode are failure typically occurs just beyond the 2 mA/quad level. The reasons for the premature failure are presumed to relate to environmental factors with the tube, such as contaminants and backscattering from tube surfaces. Other factors, of course, affect the appropriateness of FEAs in a TWT; they shall be discussed in the following.

Twystrode Output Power. A twystrode extracts power from the electron beam by passing the beam through the fields of an electromagnetic wave propagating with a phase velocity slightly lower than the beam velocity (90), as shown in Fig. 1(b). On casual inspection, a twystrode circuit closely resembles a TWT output section: optimizing the circuit impedance leads to the same specifications for beam and circuit radii. When the electron beam is density modulated, special consideration must be given to the gradual reduction of the phase velocity along the length of the circuit ("tapering") in order to optimize power extraction and the quality of the spent beam. In tapering, the phase velocity of the traveling-wave circuitry is reduced as the electron beam slows in order to maintain tight coupling between the traveling wave and the slowing beam. The maximum useful reduction is limited by loss of coherence in the electron bunches, which results in the reacceleration of some electrons to high energy, thereby degrading the efficiency of the collector. Tightly bunched beams enable greater total velocity tapers, as do longer circuits in which the taper occurs more gradually. Therefore increasing the efficiency of a twystrode output circuit requires compromises with the size and the gain of the amplifier.

There is no small-signal theory of the interaction of a density-modulated electron beam with a traveling-wave circuit. The modulation is typically too strong to allow a linearization of the beam current, and the beam-circuit interaction is sufficiently strong to materially alter the beam current waveform within one wave period. Therefore, a useful analysis of the efficiency of twystrodes involves PIC computations covering the full length of the circuit. In two-dimensional (2-D) calculations, the electromagnetic fields can be represented either by polarized boundary conditions (91) or by mode decomposition (92,93).

The polarizer model (91) uses a sheath approximation in which the finite-wire helix is represented as a cylindrical sheet with infinite conductance parallel to the helix wire and zero conductance in the perpendicular direction. This representation, which is realized as a boundary condition on the fields, enables accurate modeling of a helical circuit in a 2-D PIC simulation. The model is implemented in MAGIC as a projection operator that constrains axial and azimuthal fields at the helix radius. Special diagnostics have been developed to analyze fundamental mode power as a function of axial distance. This model has been in use for several years and has been successfully tested against the series of EGA experiments (94).

Investigations of FEA twystrodes are underway at laboratories in the United States (22) and Japan. Although no report of a density-modulated electron beam in a traveling-wave output circuit has yet appeared, NEC Corporation has reported a velocity-modulated TWT with an FEA cathode (17,18,19).

Likely Research Directions

Gated-FEA cathodes have operational characteristics (e.g., small size, density modulation, high cutoff frequency, and instant-on capability) that should enable superior performance in microwave inductive output amplifiers. Furthermore, both the modulation of FEAs at microwave frequencies is possible and sufficiently high emission currents have been experimentally demonstrated in clean and well-controlled environments. Future research in this area must therefore center on the development of FEAs that will perform reliably in a tube environment. This endeavor can be divided into two thrusts, improving the processes and materials with which FEAs are fabricated and accommodating the instabilities that remain with the best available current technology.

A proper approach to the first of these areas requires a systematic and scientifically supportable study of tip and gate materials. It is not clear that currently (1999) available physical diagnosis techniques are capable of such a task. The dimensions of the structures that provide field emission are at least as small as 100 Å, and may indeed be even smaller, in view of the possibility that nanoprotrusions provide the true emission centers on microtips. Studies of advanced materials, such as the carbides, need to continue, and such investigations must be constantly mindful of the requirements for FEA cathodes, for example, low gate current and high packing density. FEA stabilization may well be the best near-term solution to the problem. Current-limiting techniques using both resistive and active devices, along the lines of the VECTL approach of NEC, should be investigated.

It is almost paradoxical, and certainly frustrating, that the application of gated FEAs to the microwave tube, the application that spawned the field of vacuum microelectronics, has yet to be convincingly demonstrated. It is evident that the operation of real-life FEAs is quite complex, and this complexity has thus far thwarted several concerted efforts to insert a gated FEA cathode into a microwave tube. Nevertheless, much progress has been made. It is clear that the insertion of a gated FEA cathode into a microwave amplifier tube is within the grasp of the technical community.

BIBLIOGRAPHY

1. F. M. Charbonnier, *et al.* Basic and applied studies of field emission at microwave frequencies, *Proc. IEEE* **51**: 991–1004, 1963.
2. I. Brodie C. A. Spindt, The application of thin film field emission cathodes to electronic tubes, *Appl. Sur. Sci.* **2**: 149–163, 1979.
3. C. A. Spindt, *et al.* Field emitter arrays applied to vacuum fluorescent display, *IEEE Trans. Electron Devices* **36**: 225–228, 1989.
4. C. A. Spindt, *et al.* Field emitter arrays for vacuum microelectronics, *IEEE Trans. Electron Devices* **38**: 2355–2363, 1991.
5. J. D. Levine, *et al.* Field emission from microtip test arrays using resistor stabilization, *J. Vac. Sci. Technol. B* **13**: 474–477, 1995.
6. K. Yokoo, *et al.* Active control of the emission current of field emitter arrays, *J. Vac. Sci. Technol. B* **13**: 491–493, 1995.
7. J. D. Levine, Statistical analysis of field emitter emissivity: Application to flat displays, *J. Vac. Sci. Technol. B* **13**: 553–557, 1995.
8. J. D. Levine, Benefits of the lateral resistor in a field effect display, *J. Vac. Sci. Technol. B* **14**: 2008–2010, 1996.
9. J. M. Kim, *et al.* Parameters for improving reliability of full color field emission display devices, *J. Vac. Sci. Technol. B* **16**: 736–740, 1998.
10. J. M. Early, Maximum rapidly-switchable power density in junction triodes, *IRE Trans. Electron. Devices* **ED-6**: 322–325, 1959.
11. E. O. Johnson, Physical limitation on frequency and power parameters of transistors, *RCA Rev.* **26**: 163–177, 1965.

12. D. B. Hamilton, J. K. Knipp, J. B. H. Kuper, *Klystrons and Microwave Triodes*, Rad. Lab. Ser., Vol. 7, Chaps. 1, 2, and 6.
13. J. A. Morton, A microwave triode for radio relay, *Bell Labs. Rec.* **27**: 166–170, 1949.
14. J. A. Morton R. M. Ryder, Design factors of the Bell Telephone Laboratories 1553 triode, *Bell Syst. Tech. J.* **29**: 496–530, 1950.
15. A. E. Bowen W. W. Mumford, A new microwave triode: Its performance as a modulator and as an amplifier, *Bell Syst. Tech. J.* **29**: 531–557, 1950.
16. M. Garven, *et al.* Field emission array experiments relevant to cold cathode gyrotrons, *Vacuum* **45**: 513–517, 1994.
17. H. Takemura, *et al.* A novel vertical current limiter fabricated with a deep trench forming technology for highly reliable field emitter arrays, *IEDM Tech. Dig.*, pp. 709–717, 1997.
18. H. Imura, *et al.* Electron gun design for traveling wave tubes (*TWTs*) using a field emitter array (*FEA*) cathode, *IEDM Tech. Dig.*, p. 721, 1997.
19. H. Makishima, *et al.* Remarkable improvement of microwave electron tubes through the development of the cathode materials, *Tech. Digest 10th IVMC*, Kyongju, Korea 1997, Seoul: (EDIRAK, 1997), pp. 194–199.
20. D. R. Whaley, *et al.* PPM focused TWT using a field emitter array cold cathode, *Proc. IEEE Int. Conf. Plasma Sci.*, Raleigh, NC, pp. 125–126, 1998.
21. C. A. Spindt, *et al.* Field-emitter-array development for microwave applications, *J. Vac. Sci. Technol. B* **14**: 1986–1989, 1996.
22. M. A. Kodis, *et al.* Optimization of field emission arrays for inductive output amplifiers, *J. Vac. Sci. Technol. B* **14**: 1990–1993, 1996.
23. C. A. Spindt, *et al.* Field-emitter-array development for high-frequency operation, *J. Vac. Sci. Technol. B* **11**: 468–473, 1993.
24. A. V. Haeff L. S. Nergaard, A wide-band inductive output amplifier, *Proc. IRE* **28**: 126–130, 1940.
25. R. H. Fowler L. W. Nordheim, Electron emission in intense electric fields, *Proc. R. Soc. London, Ser. A* **119**: 173–181, 1928.
26. C. A. Spindt, *et al.* Physical properties of thin film field emission cathodes, *J. Appl. Phys.* **47**: 5248–5263, 1976.
27. D. Nicolaescu, Physical basis for applying the Fowler-Nordheim J-E relationship to experimental I-V data, *J. Vac. Sci. Technol. B* **11**: 392–395, 1993.
28. I. Brodie P. R. Schwoebel, Vacuum microelectronic devices, *Proc. IEEE* **82**: 1006–1034, 1994.
29. C. A. Spindt, A thin film field emission cathode, *J. Appl. Phys.* **39**: 3504–3505, 1968.
30. I. Brodie C. A. Spindt, Vacuum microelectronics, *Adv. Electron. Electron Phys.* **83**: 1–106, 1992.
31. C. O. Bozler, *et al.* Arrays of gated field-emitter cones having 0.32 μm tip-to-tip spacing, *J. Vac. Sci. Technol. B* **12**: 629–632, 1994.
32. C. O. Bozler, *et al.* Field-emitter arrays for microwave power tubes, *Proc. IEEE Int. Conf. Plasma Sci.*, San Diego, CA, 1996, pp. V-13–V-16.
33. R. A. Murphy, *et al.* Fabrication of field-emitter arrays for inductive output amplifiers, *Proc. IEEE Int. Conf. Plasma Sci.*, San Diego, CA, 1997, pp. 127–131.
34. S. Itoh, *et al.* Experimental study of field emission properties of the Spindt-type field emitter, *J. Vac. Sci. Technol. B* **13**: 487–490, 1995.
35. C. T. Sune, G. W. Jones, D. G. Velenga, Fabrication of encapsulated silicon-vacuum field-emission transistors and diodes, *J. Vac. Sci. Technol. B* **10**: 2984–2988, 1992.
36. W. D. Palmer, *et al.* Measured DC performance of large arrays of silicon field emitters, *IEEE Trans. Electron Devices* **41**: 1867–1870, 1994.
37. W. D. Palmer, *et al.* Silicon field emitter arrays with low capacitance and improved transconductance for microwave amplifier applications, *J. Vac. Sci. Technol.* **13**: 576–579, 1995.
38. F. Ducroquet, *et al.* Fabrication and emission characteristics of GaAs tip and wedge-shaped field emitter arrays by wet etching, *J. Vac. Sci. Technol.* **16**: 787–789, 1998.
39. R. D. Underwood, *et al.* GaN field emitter array diode with integrated anode, *J. Vac. Sci. Technol.* **16**: 822–825, 1998.
40. T. Kozawa, *et al.* Fabrication of GaN field emitter arrays by selective area growth technique, *J. Vac. Sci. Technol.* **16**: 833–835, 1998.
41. C. E. Holland, A. Rosengreen, C. A. Spindt, A study of field emission microtriodes, *IEEE Trans. Electron Devices* **38**: 2368–2377, 1991.
42. M. S. Mousa, *et al.* Observations of work function changes in field-emitter arrays, *Appl. Surf. Sci.* **67**: 56–58, 1993.

43. S. Meassick H. Champaign, Influence of fill gases on the failure rate of gated silicon field emitter arrays, *J. Vac. Sci. Technol.* **14**: 1914–1917, 1996.
44. J. T. Trujillo, A. G. Chakhovski, C. E. Hunt, Effects of vacuum conditions on low frequency noise in silicon field emission devices, *J. Vac. Sci. Technol. B* **15**: 401–404, 1997.
45. V. T. Binh, N. Garcia, S. T. Purcell, Electron field emission from atom-sources: fabrication, properties, and applications of nanotips, in P. W. Hawkes (ed.), *Advances in Imaging and Electron Physics*, New York: Academic Press, 1996, Vol. 95, pp. 63–153.
46. V. T. Binh, *et al.* Local heating of single-atom protrusion tip during electron emission, *Surf. Sci. Lett.* **279**: L197–L201, 1992.
47. V. T. Binh, *et al.* Field-emission electron spectroscopy of single-atom tips, *Phys. Rev. Lett.* **69**: 2527–2530, 1992.
48. S. T. Purcell, V. T. Binh, R. Baptist, Nanoprotrusion model for field emission from integrated microtips, *J. Vac. Sci. Technol. B* **15**: 1666–1677, 1997.
49. L. Parameswaran, private communication.
50. M. J. Buckingham, *Noise in Electronic Devices and Systems*, New York: Wiley, 1983.
51. M. J. Kirton M. J. Uren, Noise in solid-state microstruc-tures: A new perspective on individual defects, interface state and low frequency (1/f) noise, in P. W. Hawkes (ed.), *Advances in Electron Physics*, New York: Academic Press, 1989, Vol. 38, pp. 367–468.
52. R. N. Amirkhanov, S. S. Ghots, R. Z. Bakhtizin, Autocorrelation function of 1/f current fluctuations in vacuum devices, *J. Vac. Sci. Technol. B* **14**: 2135–2137, 1996.
53. C. D. Child, Discharge from hot CaO, *Phys. Rev.* **32**: 492–511, 1911.
54. I. Langmuir, The effect of space charge and initial velocities on the potential distribution and thermionic current between parallel plane electrodes, *Phys. Rev.* **21**: 419–431, 1923.
55. K. L. Jensen, *et al.* Space charge effect on the current-voltage characteristics of gated field emitter arrays, *J. Appl. Phys.* **82**: 845–854, 1997.
56. J. P. Calame, H. F. Gray, J. L. Shaw, Analysis and design of microwave amplifiers employing field-emitter arrays, *J. Appl. Phys.* **73**: 1485–1503, 1993.
57. S. Ramo, J. R. Whinnery, T. van Duzer, *Fields and Waves in Communication Electronics*, New York: Wiley, 1965.
58. R. E. Collin, *Foundations for Microwave Engineering*, New York: McGraw-Hill, 1966.
59. M. Abramowitz I. A. Stegun, *Handbook of Mathematical Functions*, New York: Dover, 1965.
60. J. E. Rowe, A large-signal analysis of the traveling-wave amplifier: Theory and general results, *IRE Trans. Electron Devices*, **ED-3**: 39–56, 1956.
61. Y. Y. Lau D. Chernin, A review of the ac space-charge effect in electron-circuit interactions, *Phys. Fluids B: Plasma Phys.* **4**: 3473–3497, 1992.
62. H. P. Freund, E. G. Zaidman, T. M. Antonsen, Theory of helix traveling wave tubes with dielectric and vane loading, *Phys. Plasmas* **3**: 3145–3161, 1996.
63. D. N. Smithe, *et al.* Predicting twystrode output performance, *Proc. IEEE Int. Conf. Plasma Sci.*, Madison, WI, 1995, p. 297.
64. J. P. Barbour, *et al.* Space-charge effects in field emission, *Phys. Rev.* **92**: 45–51, 1953.
65. W. A. Anderson, Role of space charge in field emission cathodes, *J. Vac. Sci. Technol. B* **11**: 383–386, 1993.
66. Y. Y. Lau, Y. Liu, R. K. Parker, Electron emission: From the Fowler–Nordheim relation to the Child–Langmuir law, *Phys. Plasmas* **1**: 2082–2085, 1994.
67. L. Yun-Peng L. Enze, Space charge of field emission triode, *Appl. Surf. Sci.* **76/77**: 7–10, 1994.
68. K. L. Jensen, *et al.* Electron emission from a single Spindt-type emitter: Comparison of theory with experiment, *Appl. Surf. Sci.* **111**: 204–212, 1997.
69. W. P. Dyke, *et al.* The field emission initiated vacuum arc. I. Experiments on arc initiation, *Phys. Rev.* **91**: 1043–1054, 1953.
70. W. W. Dolan, W. P. Dyke, J. K. Trolan, The field emission initiated vacuum arc. II. The resistively heated emitter, *Phys. Rev.* **91**: 1054–1057, 1953.
71. G. N. Fursey, Field emission and vacuum breakdown, *IEEE Trans. Electr. Insul.* **EI-20**: 659–697, 1985.
72. G. N. Fursey D. V. Glazanov, Field emission properties of ultrasmall Zr spots on W, *J. Vac. Sci. Technol. B* **13**: 1044–1049, 1995.

73. W. B. Nottingham, Remarks on energy losses attending thermionic emission of electrons from metals, *Phys. Rev.* **59**: 906–907, 1941.
74. F. Charbonnier, Developing and using the field emitter as a high intensity electron source, *Appl. Surf. Sci.* **94/95**: 26–43, 1996.
75. H. S. Carslaw J. C. Jeager, *Conduction of Heat in Solids*, 2nd ed., London: Oxford University Press, 1959.
76. M. G. Ancona, Thermomechanical analysis of failure of metal field emitters, *J. Vac. Sci. Technol. B* **13**: 2206–2214, 1995.
77. M. G. Ancona, Modeling of thermal effects in silicon field emitters, *J. Vac. Sci. Technol. B* **14**: 1918–1922, 1996.
78. R. Baptist, F. Bachelet, C. Constancias, Microtips and resistive sheet: A theoretical description of the emissive properties of this system, *J. Vac. Sci. Technol. B* **15**: 385–390, 1997.
79. H. C. Miller, Surface flashover of insulators, *IEEE Trans. Electr. Insul.* **24**: 765–786, 1989.
80. W. A. Mackie, R. L. Harman, P. R. Davis, High current density field emission from transition metal carbides, *Appl. Surf. Sci.* **67**: 29–35, 1993.
81. W. A. Mackie, T. Xie, P. R. Davis, Field emission from carbide film cathodes, *J. Vac. Sci. Technol. B* **13**: 2459–2463, 1995.
82. M. L. Yu, *et al.* Improved emission stability of carbonized HfC (100) and ultrasharp W field emitters, *J. Vac. Sci. Technol. B* **13**: 2436–2440, 1995.
83. R. W. Pryor, Carbon-doped boron nitride cold cathodes, *Appl. Phys. Lett.* **68**: 1802–1804, 1996.
84. H. H. Busta R. W. Pryor, Electron emission from a laser ablated and laser annealed BN thin film emitter, *J. Appl. Phys.* **82**: 5148–5153, 1997.
85. W. Shockley, Current to conductors induced by a moving point charge, *J. Appl. Phys.* **9**: 635–636, 1938.
86. K. Nguyen, *et al.* Analysis of the 425-MHz klystrode, *IEEE Trans. Electron Devices* **38**: 2212–2220, 1991.
87. B. Goplen, *et al.* User-configurable MAGIC Code for electromagnetic PIC calculations, *Comput. Phys. Commun.* **87**: 54–86, 1995.
88. D. H. Preist M. B. Shrader, A high power klystrode with potential for space application, *IEEE Trans. Electron Devices* **38**: 2205–2211, 1991.
89. S. G. Bandy, *et al.* Application of gated field emitter arrays in microwave amplifier tubes, *Proc. IEEE Int. Conf. Plasma Sci.*, San Diego, CA, 1997, pp. 132–133.
90. K. L. Jensen, An analytical model of an emission-gated twystrode using a field emitter array, *J. Appl. Phys.* **83**: 7982–7992, 1998.
91. J. R. Pierce, *Travelling Wave Tubes*, Princeton, NJ: Van Nostrand, 1950, Chap. III and Appendix II.
92. D. Smithe, G. Warren, B. Goplen, A helix polarization model for 2-D particle-in-cell simulation of helix traveling wave tubes, *Bull. Am. Phys. Soc.* **37** (6): 297, 1992.
93. H. P. Freund E. G. Zaidman, Nonlinear theory of collective effects in helix traveling wave tubes, *Phys. Plasmas* **4**: 3180–2301, 1997.
94. M. A. Kodis, *et al.* Emission gated amplifier, *Bull. Am. Phys. Soc.* **38** (10): 2003, 1993.

R. ALLEN MURPHY
MIT Lincoln Laboratory
MARY ANNE KODIS
Jet Propulsion Laboratory